

Upper mantle thermochemical structure from seismic–geodynamic flow models: constraints from the Lithoprobe initiative¹

H.K. Claire Perry and Alessandro Forte

Abstract: High-resolution seismic models of three-dimensional mantle heterogeneity are interpreted in terms of upper mantle thermal and compositional anomalies. These anomalies produce density perturbations that drive mantle flow and corresponding convection-related geophysical observables, such as the nonhydrostatic geoid, free-air gravity anomalies, and dynamic surface topography, and provide constraints on internal mantle density structure. The convection related observables are corrected for the isostatically compensated crustal heterogeneity and compared with those predicted by tomography-based mantle flow models. Occam inversions of the surface topography and gravity data provide inferences of the velocity–density scaling coefficients, which characterize mantle density anomalies below North America. The inferred density anomalies require simultaneous contributions from temperature and composition. The density and seismic shear velocity anomalies place constraints on the thermochemical structure of the mantle beneath the North American craton. Perturbations in the molar ratio of iron, $R = X_{\text{Fe}}/(X_{\text{Fe}} + X_{\text{Mg}})$, are used to quantify the compositional anomalies in terms of iron depletion in the sub-continental mantle. Estimates of the extent of basalt depletion in the tectosphere beneath North America are obtained. This depletion is interpreted to produce a local balance between positive chemical buoyancy and the negative thermal buoyancy that would otherwise be produced by the colder temperatures of the sub-cratonic mantle relative to its sub-oceanic counterpart.

Résumé : Des modèles tridimensionnels de sismique haute résolution de l'hétérogénéité du manteau sont interprétés en termes des anomalies thermiques et de composition du manteau supérieur. Ces anomalies perturbent la densité qui contrôle le flux dans le manteau et les observables géophysiques reliés à la convection, tels que le géoïde non hydrostatique, les anomalies gravimétriques à l'air libre et la topographie dynamique de la surface; elles fournissent de plus des limites à la structure interne de la densité du manteau. Les observables reliés à la convection sont corrigés pour l'hétérogénéité de la croûte compensée isostatiquement et ils sont comparés à ceux prédits par les modèles de flux du manteau basé sur la tomographie. Des inversions Occam de la topographie de la surface et des données gravimétriques fournissent des inférences des coefficients de proportionnalité vitesse–densité, lesquels caractérisent les anomalies de densité du manteau sous l'Amérique du Nord. Les anomalies de densité inférées demandent des contributions simultanées de température et de composition. Les anomalies de densité et de vitesse de cisaillement sismique imposent des limites à la structure thermochimique du manteau sous le craton nord-américain. Des perturbations du rapport molaire du fer, $R = X_{\text{Fe}}/(X_{\text{Fe}} + X_{\text{Mg}})$, sont utilisées pour quantifier les anomalies de composition en termes d'appauvrissement en fer dans le manteau sous-continental. Des estimations sont obtenues pour l'étendue de l'appauvrissement des basaltes dans la tectosphère sous l'Amérique du Nord. Cet appauvrissement produirait un équilibre local entre la flottabilité chimique positive et la flottabilité thermique négative, un équilibre qui aurait été autrement produit par les températures plus froides du manteau sous le craton par rapport à sa contrepartie sous l'océan.

[Traduit par la Rédaction]

Introduction

As part of the Lithoprobe initiative, Canada's multidisciplinary

geoscience project (Clowes et al. 1992), numerous seismic refraction experiments were conducted over the Canadian landmass during the past 20 years. The Lithoprobe refraction results provided the basis for revising models of Canadian crustal structure that had been previously extracted from global crustal models, such as CRUST5.1 (Mooney et al. 1998). The LITH5.0 crustal model (Perry et al. 2002) was developed as an improvement to previous models to provide better constraints on crustal structure in Canada. These constraints play an essential role in determining the density and thermochemical structure of the continental lithosphere, specifically the sub-continental lithospheric mantle (SCLM). The differences between the crustal structure in models CRUST5.1 and LITH5.0 are summarized in Fig. 1 in terms of crustal thickness variations. We note that

Received 2 March 2010. Accepted 2 March 2010. Published on the NRC Research Press Web site at cjes.nrc.ca on 30 April 2010.

Paper handled by Associate Editor R. Clowes.

H.C. Perry² and A. Forte. Centre de Recherches en Géochimie et en Géodynamique (GEOTOP), Université du Québec à Montréal, Montréal, QC H3C 3P8 Canada.

¹This article is one of a series of papers published in this Special Issue on the theme *Lithoprobe — parameters, processes, and the evolution of a continent*.

²Corresponding author (e-mail: perry.claire@uqam.ca).

the most significant differences are seen in the northern Canadian Cordillera, the central Canadian Shield, and the eastern Canadian Platform, all of which were well sampled by Lithoprobe seismic refraction surveys.

In the present paper, we review how the more refined and improved LITH5.0 crustal model is used to determine the signature of isostatically compensated crustal heterogeneity in surface topography and gravity anomalies. Removal of this crustal signal yields an improved estimate of the dynamic surface topography arising from sources in the lithosphere and underlying mantle and thus provides a fundamental constraint on the density structure of the uppermost mantle.

In addition to the dynamic surface topography, other convection-related surface observables such as free-air gravity or geoid anomalies provide constraints on the density structure of the Earth's mantle. Constraining the density structure of the uppermost mantle requires a joint analysis of the ensemble of these geophysical fields, since each provides independent constraints on the mantle density structure and each is sensitive to density anomalies at different depths in the mantle. The predicted surface topography provides an integral constraint on the uppermost mantle density structure, especially at the shortest wavelengths that are mainly sensitive to lithospheric density anomalies. The predicted free-air gravity anomalies also provide localized sensitivity in the upper mantle. In a convecting mantle the short-wavelength gravity anomalies are found to have peak sensitivity to density anomalies below the lithosphere. Investigations of the geodynamic implications of three-dimensional (3-D) mantle heterogeneity in seismic tomography models (Forte and Peltier (1987), (1991); Hager and Richards (1989); Ricard and Vigny (1989); Corrieu et al. (1994); Forte (2000), (2007)) have demonstrated that the density perturbations derived from these tomography models may be used in mantle flow predictions to yield good fits to the main convection-related observables. This is valid for the nonhydrostatic geoid, tectonic plate motions, dynamic topography at the surface, and the excess flattening or dynamic ellipticity of the core-mantle boundary (CMB) (Forte 2007).

Intrinsic to the seismic-geodynamic inversions for SCLM thermochemical structure are the assumed relationships between density and seismic velocity anomalies. These relationships are complex, since the seismic shear-wave velocity and density anomalies are both dependent on temperature, composition, and pressure (Jordan 1981; Schutt and Leshner 2006). SCLM density anomalies are highly sensitive to compositional variations, such as bulk iron content, whereas the tomography-derived shear-wave velocity anomalies are mostly sensitive to temperature variations (Forte and Perry 2000; Forte and Mitrovica 2001). The results of Röhm et al. (2000), Goes et al. (2000), Deschamps et al. (2002), and Schutt and Leshner (2006) further reinforce the conclusion that seismic shear velocities in the upper mantle are mostly sensitive to temperature. More recently, Simmons et al. (2007, 2009) confirmed that 3-D mantle models consistent with both geodynamic and seismic constraints can be found while assuming a dominance of thermal effects on shear-velocity and density anomalies throughout the mantle. These studies have furthermore shown that to infer sub-continental compositional variations,

seismic constraints on velocity anomalies must be supplemented by additional constraints on density anomalies, whose sensitivity to temperature and compositional variations are comparable. If one considers continental roots as thick, long-lived domains (e.g., Jordan 1975; Griffin et al. 2009), then they must have equilibrated thermally with adjacent mantle domains through time. This would suggest that their relatively high shear-wave velocity cannot be due to intrinsic differences in temperature alone, and that the composition of the roots must be a non-negligible factor.

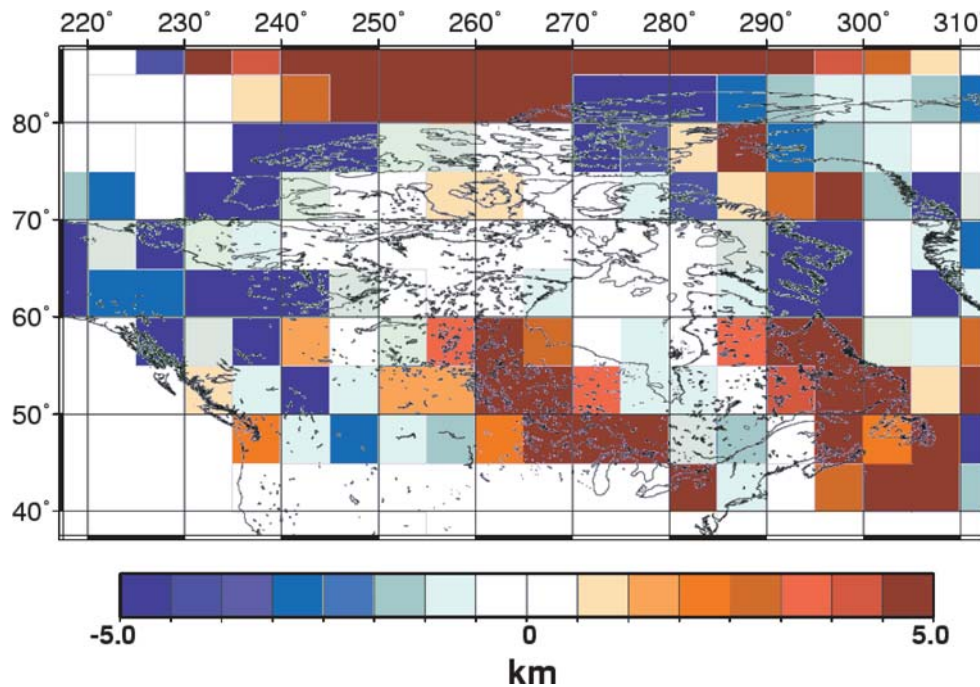
Following (Jordan 1975), we employ the term "tectosphere" to refer to the mantle below sub-continental lithosphere that is assumed to be stabilized against convective disruption by a balance between thermally generated negative buoyancy and positive chemical buoyancy. We also employ the term "dynamic topography" to signify all contributions to surface topography due to density anomalies in the mantle, including the lithosphere as well (Forte et al. 1993; Forte 2007). The observed surface topography consists of the linear superposition of the dynamic topography and the much larger amplitude topography due to the isostatic compensation of crustal heterogeneity. To obtain the dynamic contribution to the observed surface topography, the isostatic contribution is removed from the observed surface topography. The dynamic component of the observed surface topography is then used to constrain the density anomalies in the mantle. Herein lies the importance of reliable regional crustal models and the wide-ranging applications of the Lithoprobe data sets in geodynamic modelling of the continental lithosphere.

This paper reviews the methodology used for the joint seismic and geodynamic modelling of the chemical contributions to the density field in the uppermost mantle and is focussed on the North American tectosphere. We interpret the shear-wave velocity anomalies in terms of compositional variations using additional constraints from geodynamic data sets on lithospheric density structure. Specifically, we use the crust-corrected dynamic topography and free-air gravity anomalies over North America to constrain the density structure of the underlying tectosphere. This work reviews the main results from two previous papers: Forte and Perry (2000) and Perry et al. (2003), that present global and regional-scale analyses of the thermochemical structure of the tectosphere. Although this paper largely provides a synthesis of our previous work, there have been recent efforts to jointly invert seismic and geodynamic data (Simmons et al. 2006) that have led to revised estimates of the density and buoyancy structure of continental roots (Simmons et al. 2007). The implications of these newer studies will also be discussed in the context of the earlier results.

Buoyancy of continents and compositional and thermal structure

The accumulated evidence from numerous geological and geophysical studies suggests that cratons have been stable since Archean times, and that they are underlain by thick, cold, and stiff mantle roots largely preserved against convective disruption since their initial formation. Both geochemical analyses and thermodynamic arguments support the stability of cratons over billion-year time scales (e.g.,

Fig. 1. The difference in crustal thickness between models LITH5.0 (Perry et al. 2002) and CRUST5.1 (Mooney et al. 1998). The average root mean square (rms) difference in regions constrained by Lithoprobe data is found to be 5.5 km. In general, model CRUST5.1 underestimates the thickness of the crust in parts of the central Canadian Shield and overestimates crustal thickness in regions of the northern Canadian Cordillera.



Pearson 1999; Mareschal and Jaupart 2006). It is assumed that the high viscosity of the cratonic roots, owing to their colder temperatures, protects them from large-scale deformation, however, the fact that they are cold and thick, also suggests that they are dense and gravitationally unstable. The stability of such thick, cold cratonic roots over billion-year time scales requires some source of positive buoyancy to oppose the thermally generated instability. Depleted sub-continental lithosphere has less iron and garnet than fertile mantle and, therefore, has a lower intrinsic density and higher seismic velocity (Jordan 1975, 1978, 1979; Lee 2003). The process of basalt extraction from fertile peridotite produces a residuum of depleted mantle material that is chemically more buoyant relative to the surrounding mantle, and this is believed to be the mechanism responsible for the formation of the upper 200 km of the Archean lithosphere (Boyd and Callister 1976; Jordan 1979; Jaques 1987; Sobolev 1987). The dynamic equilibrium between the competing effects of positive chemical buoyancy and the opposing negative thermal buoyancy is believed to be a determining factor for the stability of cratons over long geological time scales, and this work investigates this outstanding question from a geodynamic perspective.

Seismic and petrologic data suggest the presence of a sub-continental chemical boundary layer (CBL), whose base may or may not be coincident with the base of the thermally and rheologically defined lithospheric mantle (Jordan 1981; Snyder et al. 2004; O'Reilly and Griffin 2006; Griffin et al. 2009). Global and regional models of seismic tomography

suggest high-velocity roots below continents extend to depths between 200 and 400 km (Grand 2002; van der Lee and Nolet 1997; Ekström and Dziewonski 1998; Li et al. 1998; Fischer and van der Hilst 1999; Zhao et al. 1999; Mégnin and Romanowicz 2000; Ritsema and van Heijst 2000; Godey et al. 2004; Nettles and Dziewonski 2008) and they show that the sub-cratonic mantle is characterized by shear-wave speeds at least 5% faster than the ambient mantle. Global studies of the structure of the continental and oceanic lithospheres using geoid anomalies and heat flow suggest the presence of a chemically and petrologically distinct reservoir beneath cratons (Forte et al. 1995; Doin et al. 1996; Forte and Perry 2000; Perry et al. 2003; van Gerven et al. 2004). Studies based on continental heat flow and gravity data suggest that the tectosphere thermal boundary layer may extend deeper, between 200 and 330 km depth (Doin et al. 1996; Jaupart and Mareschal 1999). Studies of mantle xenoliths (Finnerty and Boyd 1987; Rudnick et al. 1998), mantle xenocrysts (Griffin et al. 2004; O'Reilly and Griffin 2006; Griffin et al. 2009), diamondiferous kimberlites (Boyd et al. 1985), and surface heat flow (Jaupart and Mareschal 1999; Mareschal et al. 2000) suggest that cratonic mantle temperatures are anomalously low and relatively consistent with the high seismic velocities observed beneath cratons.

Archean SCLM is strongly depleted in basaltic components and is highly magnesian (Jordan 1981) in composition. It is a zone consisting mainly of ultramafic rocks, ranging from lherzolites to dunites and harzburgites (Griffin et al. 2009), a compositional range generally interpreted in terms

of progressive removal of the basaltic components during partial melting (Jordan 1981). Well-studied xenolith and xenocryst suites suggest that Archean SCLM is composed principally of depleted garnet lherzolites with a high orthopyroxene/olivine ratio. However, Griffin et al. (2009) suggest that most Archean SCLM originally consisted of highly depleted dunites and harzburgites and that incorporation of these rocks into the upper parts of cratonic SCLM better satisfies the seismic and gravity data. It should be noted that most North American Archean SCLM, with the exception of the Slave Province, appears to be less depleted than similar sections that have been extensively studied in the southern African and Siberian cratons. According to analysis of peridotitic garnet xenocrysts from kimberlites and other volcanic rocks, the Slave Province SCLM shows a two-layer structure, where the upper layer is ultradepleted and thick (~150 km) and the lower layer is less depleted and metasomatized (Griffin et al. 2004; O'Reilly and Griffin 2006).

Re-evaluation of petrological analysis of xenolith and xenocryst suites from kimberlitic zones in cratons worldwide suggests that fertile SCLM may be even more depleted than previously suggested. Global and regional seismic tomography indicate that most kimberlites cluster at the peripheries of high-velocity *S*-wave zones of the cratons and are thus likely representative of more strongly refertilized SCLM (Begg et al. 2009). Thus, preferential sampling of kimberlites at the peripheries of the cratons (and not generally within their interiors) has biased our estimates of fertile SCLM composition toward metasomatized material (Griffin et al. 2009). These results suggest that pristine SCLM consists of highly depleted dunites and harzburgites and that the upper 100–150 km of the tectosphere is more strongly depleted than the garnet lherzolites previously accepted as representative of Archean SCLM (Griffin et al. 2009).

These petrological studies indicate a refractory mantle root beneath the North American craton, which would suggest an overlying enriched Archean crust, if crust and mantle have remained mechanically coupled through time. Indeed, a secular variation in the composition of SCLM (less basaltic depletion through time) is evident from petrological analysis of garnet xenolith and xenocryst suites when SCLM age is based on the tectonothermal age of the overlying crust (O'Reilly and Griffin 2006; Griffin et al. 2009). A similar secular variation in basalt depletion of SCLM, more specifically in the tectosphere, seems evident from the present geodynamic inversions.

Geodynamic data sets

Here, we present the geodynamic data sets used to place constraints on the tectosphere density structure. The first step in retrieving the surface constraints on the viscous response of the convecting mantle is the removal of the crustal signal from the observed gravity and topography data sets to estimate the isostatic contribution to these observed fields. The difference between the observed and predicted isostatic components of these data is the contribution associated with density perturbations throughout Earth's mantle (including the lithosphere).

In the joint inversions discussed in the following sections,

we employ the dynamic topography and free-air gravity anomalies in North America, and also incorporate global constraints provided by convection-related data consisting of tectonic plate velocities (DeMets et al. 1990), the satellite-observed GEM-T2 free-air gravity anomalies (Marsh et al. 1990), the global surface topography corrected for crustal isostasy (Mooney et al. 1998), and the excess ellipticity of the CMB (Mathews et al. 2002) that is inferred from the period of the Earth's retrograde free core nutation (Herring et al. 2002). The EGM96 geopotential model (Lemoine et al. 1996) is used as a constraint on the North American geoid and free-air gravity anomalies. EGM96 incorporates surface gravity anomaly measurements across North America (and other continents). The global geodynamic constraints are incorporated with the North American geodynamic data sets to constrain the density structure of the lower mantle.

Isostatic reduction of crustal contributions to geodynamic data

The condition of isostasy, or surface mass compensation, requires that the total mass in a unit-area vertical column at the surface be constant down to a compensation depth. This is the condition of hydrostatic equilibrium. It can be expressed in terms of the depth distribution of near-surface, lateral density anomalies $\Delta\rho(y)$:

$$[1] \quad \int_0^h \Delta\rho(y)dy = 0$$

where h is the thickness of the surface layer and y is the depth variable. To isolate the mantle or dynamic contribution to surface geodynamic observables, it is necessary to remove the isostatically compensated crustal contribution that satisfies condition [1].

Isostatic surface topography

The condition of isostasy in eq. [1] is applied to the crustal model to determine the isostatic surface topography. The crustal thickness and velocity structure in North America is taken from the LITH5.0 crustal model (Perry et al. 2002), and *P*-wave velocities are converted to densities using the velocity-to-density systematics of Christensen and Mooney (1995). The estimates of isostatic topography and residual dynamic topography are highly sensitive to the *P*-wave velocity-to-density conversion scheme. The root mean square (rms) amplitude of the dynamic topography signal, which is derived on the basis of the estimated isostatic topography, varies by as much as 63% within the error bounds of the linear regression lines given in Christensen and Mooney (1995). In estimating crustal densities, we consider an upper crustal section composed of granitic gneiss that becomes increasingly tonalitic with depth; a mid-crustal region characterized by abundant amphibolite; and a lower crustal region containing granulite-facies assemblages grading to mafic garnet granulite.

The vertical loads, $\sigma_{L5.0}$, in each of the $5^\circ \times 5^\circ$ cells defined in the LITH5.0 model are calculated using

$$[2] \quad \int_0^h \rho(y)dy = \sigma_{L5.0}$$

where h is the crustal thickness in each cell. For the

LITH5.0 cells (where Lithoprobe data have replaced CRUST5.1 data), the vertical loads σ defined in eq. [2] are calculated using a point-by-point vertical integration of density through the crust, instead of the layer-by-layer scheme required by the CRUST5.1 model. Therefore, in calculating σ in cells containing Lithoprobe data, we spline integrate ρ through a maximum of five depth nodes, depending on the velocity model in the each cell. To each σ , we then add the additional surface load corresponding to sedimentary layers, water, and ice based on the CRUST5.1 model (Mooney et al. 1998).

The isostasy principle reduces to the determination of the (hydrostatic) equilibrium depths of the Mohorovičić discontinuity (Moho), the solid surface, and all intermediate crustal boundaries (which define the upper, middle, and lower crust). Using the boundary locations in the individual cells, we define global horizontal averages, denoted by the symbol $\langle \rangle$, for the boundary locations. All perturbations are defined relative to the global averages. The perturbation of the crustal thickness in each cell is defined by

$$[3] \quad \delta H_C(\theta, \phi) = H_C(\theta, \phi) - \langle H_C \rangle$$

where $H_C(\theta, \phi)$ is the local crustal thickness and $\langle H_C \rangle$ is the corresponding global average.

The vertical loads, $\sigma_{L5.0}$, in the Lithoprobe data cells are then used to solve for the perturbation of the Moho satisfying the isostatic condition in eq. [1]. This translates into determining the vertical distance that the crust will sink into the mantle (and the vertical distance to which the mantle will be displaced) to maintain isostatic equilibrium. The perturbation of the Moho is defined as

$$[4] \quad \delta M_{L5.0}(\theta, \phi) = \frac{\langle \sigma_{L5.0} \rangle - \sigma_{L5.0}(\theta, \phi)}{\rho_{um}}$$

where $\rho_{um} = 3.36 \text{ Mg/m}^3$ is the global-average, upper-mantle (sub-Moho) density in preliminary reference Earth model (PREM, Dziewonski and Anderson 1981). We assume a laterally homogeneous sub-Moho density ρ_{um} as required for the mantle to be in a state of hydrostatic equilibrium (i.e., surfaces of constant density must coincide with surfaces of constant pressure). The isostatic surface topography is solved using eqs. [3] and [4]:

$$[5] \quad \delta a_{iso}(\theta, \phi) = \delta M_{L5.0}(\theta, \phi) + \delta H_C(\theta, \phi)$$

For cells containing CRUST5.1 data, we denote local and horizontally averaged thickness and density pairs, corresponding to a crustal layer, i , by (h_i, ρ_i) and $\langle h_i, \rho_i \rangle$, respectively. In the cells where only CRUST5.1 data exist, we vertically integrate the density in seven layers (three crust, two sediment, one water, and one ice). The total vertical loads in each $5^\circ \times 5^\circ$ cell are calculated by summing $N = 7$ thickness–density pairs to find the Moho perturbation. In analogy to eq. [4], the condition of isostasy applied to the CRUST5.1 model yields

$$[6] \quad \delta M_{C5.1}(\theta, \phi) = \frac{\sum_{i=1}^N \langle \sigma_{C5.1i} \rangle - \sum_{i=1}^N \sigma_{C5.1i}(\theta, \phi)}{\rho_{um}}$$

where $\langle \sigma_{C5.1i} \rangle = \langle \rho_i, h_i \rangle$.

The lateral variations in isostatic surface topography (rel-

ative to a global mean value of zero) is then solved as in eq. [5]:

$$[7] \quad \delta a_{iso}(\theta, \phi) = \delta M_{C5.1}(\theta, \phi) + \delta H_C(\theta, \phi)$$

Figure 2(a) shows the observed ETOPO-5 surface topography (National Geophysical Data Center 1988) in kilometres. Figure 2(b) shows the isostatic surface topography for North America calculated on the basis of eqs. [4] and [6]. The amplitude of its signal is comparable to that of the observed surface topography, however its shape is influenced by the crustal structure and thickness (see fig. 3a in Perry et al. (2002)). The crustal model is re-sampled to a $2^\circ \times 2^\circ$ grid for use with the seismic tomography model of Grand (2002).

Isostatic geoid anomalies

The geoid height anomalies, ΔN , produced by the isostatically supported crustal density anomalies are calculated following the method of Turcotte and Schubert (1982), where geoid anomalies are directly proportional to the vertical dipole moment of the density anomalies

$$[8] \quad \Delta N = -\frac{2\pi G}{g_0} \int_0^h y \Delta \rho(y) dy$$

where G is the gravitational constant, g_0 is the gravitational acceleration, h is the thickness of each crustal block, and $\Delta \rho(y)$ are the lateral perturbations in density as a function of depth. The anomaly defined in eq. [8] may be called the isostatic geoid, since it assumes perfect compensation as defined by expression [1]. This assumption of complete compensation is valid in the long-wavelength limit, in which the horizontal scale length of crustal heterogeneity is assumed much greater than the thickness of the crustal blocks and the thickness of the elastic lithosphere. In this case, flexural response of the elastic lithosphere thickness may then be ignored. The residual (or dynamic) geoid anomalies are estimated by subtracting the isostatic geoid from the corresponding observed field and reflect all density anomalies from mantle sources.

The corresponding isostatic free-air gravity anomalies are obtained from eq. [8] using the following expression (see Appendix A):

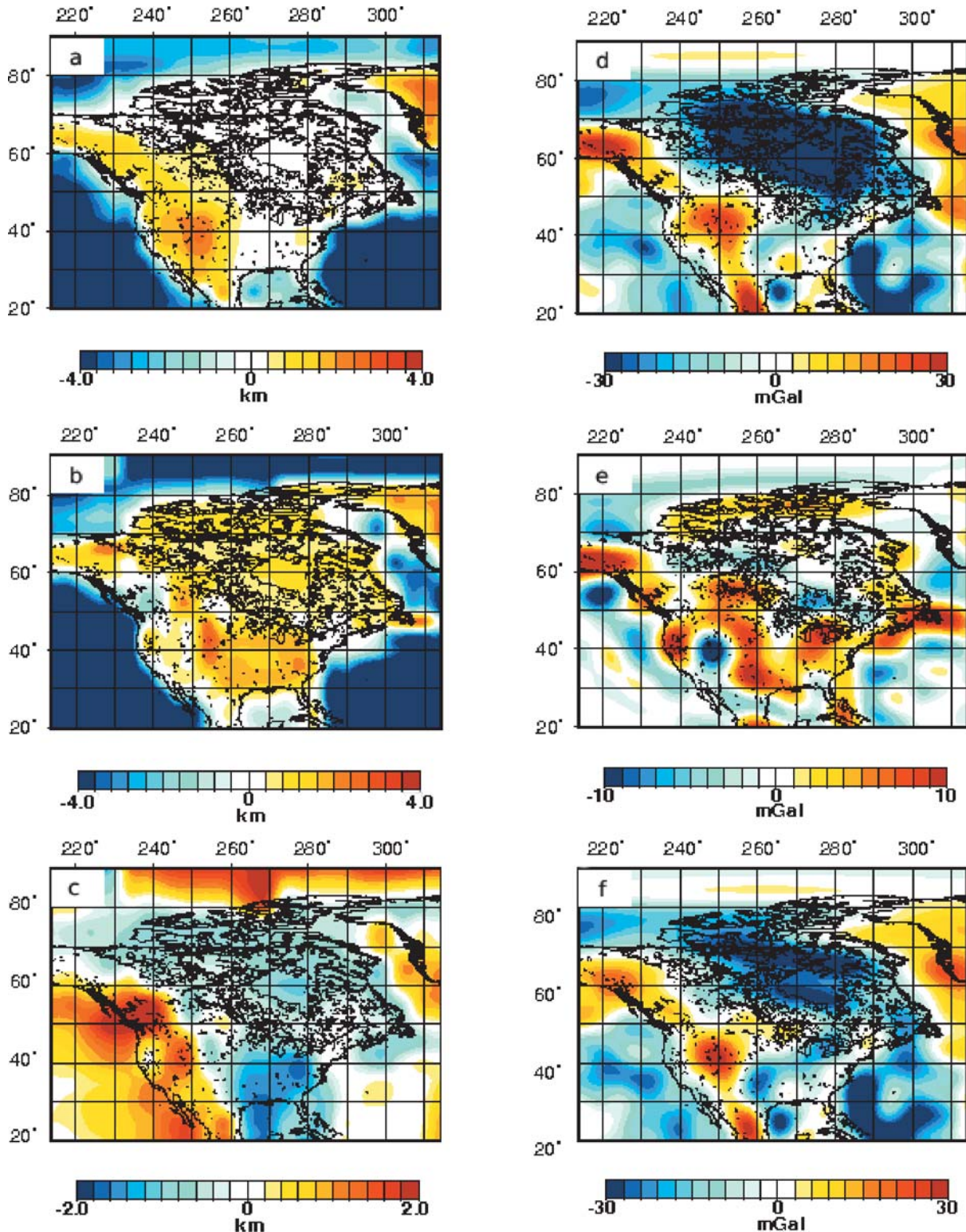
$$[9] \quad \Delta G(\theta, \phi) = -\left[\frac{\partial \Delta N}{\partial r} \right]_{R_0} - \frac{2}{R_0} \Delta N$$

in which $R_0 = 6371 \text{ km}$ is Earth’s mean radius and all terms are calculated in the spherical harmonic domain (see eq. [A4]). The anomalies in Fig. 2(e), synthesized from harmonic coefficients in the degree range $\ell = 2\text{--}36$, are of the order of $\sim 50 \text{ mGal}$, and show a large negative anomaly centred over Hudson Bay. The isostatic component provides as much as 20% of the total gravity signal and, thus, as in the case of the geoid anomalies, it must be removed from the observed signal to accurately constrain mantle density sources.

Glacial isostasy

The topography and free-air gravity data over North America are also corrected for the effects arising from the incomplete rebound of the surface following the Laurentide

Fig. 2. (a) Observed surface topography of North America from the ETOPO-5 compilation. (b) Isostatic surface topography calculated on the basis of a recent compilation of crustal thickness and velocity structure (Perry et al. 2002). (c) The residual or dynamic surface topography, obtained by subtracting the isostatic topography in (b) from that observed in (a). (d) Free-air gravity anomalies from the EGM96 compilation (Lemoine et al. 1996) obtained using the relation in eq. [A4] in Appendix A). (e) Isostatic free-air gravity anomalies calculated on the basis of a recent compilation of crustal thickness and velocity structure (Perry et al. 2002) and eq. [A4]). (f) The residual or dynamic free-air gravity anomalies obtained by subtracting the isostatic free-air gravity anomalies in (e) from those observed in (d). All fields are represented as averages in the $5^\circ \times 5^\circ$ cells.



deglaciation event. For example, the large free-air gravity low over Hudson Bay is associated in part to ongoing post-glacial rebound, with the remaining contribution provided by mantle convection (Peltier et al. 1992). The relative importance of the rebound signal compared with the mantle dynamics signal below North America is still under debate (e.g., Mitrovia 1997; Simons and Hager 1997). Analysis of time-dependent gravity data from the Gravity Recovery and Climate Experiment (GRACE) satellite mission now suggests that the gravity anomalies in Hudson Bay due to incomplete glacial isostatic adjustment are ~ -15 mGal (Tamisiea et al. 2007; $1 \text{ Gal} = 1 \text{ cm s}^{-2}$). We use an earlier calculation of the post-glacial rebound signal calculated using a model of a viscoelastic self-gravitating sphere (Mitrovia and Tamisiea, personal communication). The rebound signal is estimated using a simple two-layer approximation of the viscosity profile in the mantle, where the viscosity of the upper and lower mantle is $0.3 \times 10^{21} \text{ Pa s}$ and $20 \times 10^{21} \text{ Pa s}$, respectively. An elastic lithosphere of thickness 96 km is assumed. This model provides an estimate of the present-day radial displacement of the surface (related to non-relaxed topography) and the component of the observed free-air gravity data resulting from post-glacial rebound processes. The peak (negative) value of the free-air gravity anomalies predicted over Hudson Bay is about -19 mGal and is comparable to the most recent estimate by Tamisiea et al. (2007).

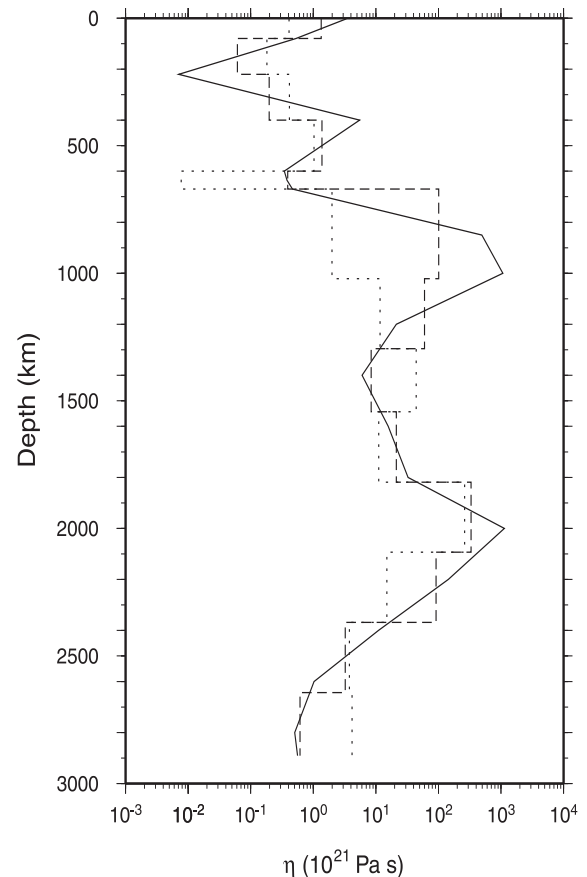
Methods

The density perturbations in the North American tectosphere are constrained using the mantle flow theory presented in the following section and a seismically inferred 3-D model of mantle structure. The flow theory is based on geodynamic kernels, which relate the viscous response of the mantle to internal density perturbations. With the isostatic components of the surface topography and free-air gravity estimated earlier in the text, we may compare the “observed” mantle signal with the “predicted” mantle signal, representing the mantle’s dynamic response to density perturbations at different depths. The starting point of our analysis is the seismically inferred 3-D mantle structure from the tomography model of Grand (2002). The seismic velocity anomalies in this model are related to mantle density anomalies through geodynamically inferred velocity–density scaling coefficients ($d \ln \rho / d \ln V_s$), which are determined through an inversion scheme discussed later in the text. The combined seismic velocity and density anomalies may then be used to constrain the thermochemical structure of the tectosphere.

Buoyancy-induced mantle flow

The mantle flow theory for determining the viscous response of the mantle to internal density perturbations on a regional (continental) scale is summarized in Appendix A. We use a tomography-based mantle flow model to predict the dynamic topography and free-air gravity fields, which are then compared with the observed, present-day fields. The internal loading formulation of the flow theory that we employ allows for the calculation of the viscous response to density loads placed at arbitrary depths in the mantle. The

Fig. 3. Depth-dependent effective viscosity of the Earth’s mantle. The solid curve represents the viscosity profile inferred in Occam inversions (Forte and Mitrovia 2001) of the geodynamic data (listed in Table 1 based on the 3-D seismic models of Grand (2002)). The dotted line represents a recent 13-layer viscosity profile obtained by simultaneously inverting global convection and post-glacial rebound data (Mitrovia and Forte 2002). The broken line is obtained by calculating the averages of the convection viscosity inference (solid curve) in the same 13 layers as the dotted curve.



full theoretical and numerical procedure employed in solving the flow equations for an arbitrary distribution of internal density perturbations $\delta\rho(r, \theta, \phi)$ in a spherical, compressible, and self-gravitating mantle is described in and Forte and Peltier (1991) and Forte (2000, 2007).

The relationship between the flow-related observables, such as the nonhydrostatic geoid, surface topography and free-air gravity anomalies, and the internal density perturbations that drive the flow is expressed in terms of geodynamic kernel functions. The kernels relate the flow-related observables to density loads at different depths in the mantle. The kernel functions summarize the viscous response of the mantle and are dependent on the rheology of the mantle, represented here in terms of a radial viscosity profile. The kernel functions employed in this study are calculated using a reformulated viscous-flow theory (Forte 2000), in which the flow solution is dependent only on the logarithm of the depth-dependent viscosity. In Fig. 3, we present a compar-

son of an earlier inference of the depth-dependent mantle viscosity obtained solely on the basis of convection-related data sets (Forte and Mitrovica 2001). Mitrovica and Forte (2004) and a radial viscosity profile constrained by simultaneously inverting glacial isostatic adjustment (GIA) and convection data sets (Mitrovica and Forte 2002) obtained a revised inference of depth-dependent mantle viscosity from joint GIA–convection inversions that yield viscous-flow response (i.e., kernel) functions similar to those obtained on the basis of the Mitrovica and Forte (2002) inversions. The topography and geoid kernels, $Tl(r)$ and $Gl(r)$, employed here and in the following convection predictions are calculated on the basis of the effective viscosity derived from the earlier (Mitrovica and Forte 2002) inversions.

Given the high viscosity of the mantle compared with the relatively inviscid outer core, mantle flow solutions assume a simple free-slip boundary condition at the CMB. For the surface boundary conditions, we assume rigid plates which are viscously coupled to the mantle-wide convection process. The theoretical method of viscous plate-coupling developed by Forte and Peltier (1991, 1994) is used here to model the mantle flow with rigid surface plates. The flow theory is formulated such that the buoyancy-induced mantle flow is coupled to the 13 principal (rigid) surface tectonic plates (DeMets et al. 1990), whose motions are determined by the underlying flow field (Forte and Peltier 1994). This plate-coupled flow theory is employed to calculate the global convection-related data employed in the analysis presented later in the text. In the regional-scale analysis of North American data, the boundary condition may be locally approximated as an effective no-slip surface, since the density anomalies below the continent effectively interact with an overlying rigid lid.

Velocity-to-density conversion

Archean SCLM is a particularly sensitive region for determining the relationships between seismic velocity and den-

sity, due to its variable thermal structure, chemical composition, and thickness (a few tens of kilometres in rift zones to >250 km beneath some Archean cratons). A key issue in developing models of sub-continental mantle flow is the choice of velocity–density conversion factor ($d \ln \rho / d \ln V_s$), needed to translate the relative seismic shear-wave velocity perturbations ($\delta V_s / V$) into equivalent density perturbations ($\delta \rho / \rho$). We note here that Schutt and Leshner (2006) examined the effects of melt depletion on density and anharmonic temperature dependence of V_p and V_s on the basis of the melting relations of fertile peridotite between 1 and 7 GPa. They concluded that taking into account the pressure variation of the density of mantle residuum may reduce the effect of depleted upper mantle composition on V_s . In the present work, however, we use the standard temperature and pressure (STP) density and velocity values from Jordan (1979).

Forte et al. (1993, 1994) inverted gravity data for a simple depth variation in $d \ln \rho / d \ln V_s$, which was assumed to be constant in the top 400 km of the mantle, constant in the transition zone between 400 km and 670 km depth, and assumed to vary smoothly across the lower mantle. Forte and Perry (2000) and Forte and Mitrovica (2001) determined the $d \ln \rho / d \ln V_s$ conversion factors for a more complex depth variation on a global scale. In this study, we determine the $d \ln \rho / d \ln V_s$ conversion factors for each layer of the Grand (2002) model of seismic shear-wave velocity heterogeneity. The joint inversions employ the geodynamic data as constraints on the density perturbations in the mantle.

As shown in Appendix A, the global viscous-flow response of the mantle can be expressed in terms of local spatial coordinates. On the basis of the expressions for dynamic topography and free-air gravity anomalies in geographic coordinates (see eqs. [A12] and [A15]), we obtain the following equations that incorporate conversion factors and seismic velocity anomalies for two distinct regions in the mantle:

$$[10] \quad \delta a(\theta_i, \phi_j) = \sum_{k=1}^N \left\{ \left(\frac{d \ln \rho}{d \ln V_s} \right)_{\text{sh}}^k \left[\int_{r_k}^{r_{k+1}} dr \int_0^\pi \sin \theta' d\theta' \int_0^{2\pi} d\phi' T(r, \Delta_{ij}) \left(\frac{\delta V_s}{V_s} \right)_{\text{sh}} \right] \right. \\ \left. + \left(\frac{d \ln \rho}{d \ln V_s} \right)_{\text{th}}^k \left[\int_{r_k}^{r_{k+1}} dr \int_0^\pi \sin \theta' d\theta' \int_0^{2\pi} d\phi' T(r, \Delta_{ij}) \left(\frac{\delta V_s}{V_s} \right)_{\text{th}} \right] \right\}$$

and

$$[11] \quad \delta G(\theta_i, \phi_j) = \frac{3g_0}{\bar{\rho}R} \sum_{k=1}^N \left\{ \left(\frac{d \ln \rho}{d \ln V_s} \right)_{\text{sh}}^k \left[\int_{r_k}^{r_{k+1}} dr \int_0^\pi \sin \theta' d\theta' \int_0^{2\pi} d\phi' G(r, \Delta_{ij}) \left(\frac{\delta V_s}{V_s} \right)_{\text{sh}} \right] \right. \\ \left. + \left(\frac{d \ln \rho}{d \ln V_s} \right)_{\text{th}}^k \left[\int_{r_k}^{r_{k+1}} dr \int_0^\pi \sin \theta' d\theta' \int_0^{2\pi} d\phi' G(r, \Delta_{ij}) \left(\frac{\delta V_s}{V_s} \right)_{\text{th}} \right] \right\}$$

where $N = 22$ is the number of layers in the Grand (2002) model, “sh” denotes mantle beneath shields and “th” denotes mantle outside shield regions, which is presumed to be characterized mainly by thermally generated anomalies.

In the case that the mantle was a perfectly elastic and chemically homogeneous region and did not undergo pressure- or temperature-induced phase transformations, reasonable estimates for $d \ln \rho/d \ln V_s$ could be derived from laboratory measurements of the temperature derivatives of seismic velocity and density (Forte et al. 1994). However, it has been shown that the mantle may deviate significantly from this ideal behaviour (e.g., Karato 1993; Forte and Mitrovica 2001), and therefore the results of laboratory studies cannot be readily applied to the mantle without verifying the plausibility of the resulting geophysical predictions.

The density structure of the tectosphere is determined through an Occam inversion of the geodynamic data based on the theoretical relationships given in eqs. [10] and [11], in which the shear-velocity perturbations $\delta V_s/V_s$, given by the Grand (2002) model are expressed as the percent of deviation from horizontally averaged values. The shear-wave velocity heterogeneity associated with the continental root below North America is isolated such that its density may be inferred independently from the rest of the upper mantle. This is carried out by identifying those portions of the mantle lying below the North American shield which are characterized by positive shear-velocity anomalies ($\delta V_s/V_s > 0$). In doing so, we delineate the depth-dependent horizontal extent of the tectosphere and the corresponding shear-wave velocity anomalies, which we denote by $(\delta V_s/V_s)_{sh}$. The seismic velocity anomalies outside the tectosphere are denoted by $(\delta V_s/V_s)_{th}$, assuming that the seismic anomalies exterior to the tectosphere are primarily thermal in origin. The assumption that seismic anomalies outside the tectosphere are thermally induced may not be valid in tectonically active regions characterized by substantial basaltic magmatism (e.g., under the southwestern US and Basin and Range province).

Inversion method for velocity–density conversion factors

We employ the Occam inversion method (Constable et al. 1987) to infer optimal velocity–density scaling factors ($d \ln \rho/d \ln V_s$) for the mantle to satisfy the observed geodynamic fields. This method finds the model, \mathbf{m} , which minimizes the misfit between data and predictions and simultaneously minimizes a measure of model roughness. This technique delivers the smoothest radial velocity–density scaling profile that is consistent with the data. This linear inversion algorithm allows us to move arbitrarily far away from the assumed starting model since only the roughness of the profile is penalized. The goodness of fit of the model predictions to the actual values is quantified by the usual weighted least-squares criterion (Constable et al. 1987):

$$[12] \quad X^2 = \sum_{j=1}^M (d_j - F_j[\mathbf{m}])^2 / \sigma_j^2$$

where σ_j is the uncertainty in the j th datum assuming statistical independence of the errors, d_j is the j th datum, and F_j is the forward model functional associated with the j th datum. In vector notation, this functional dependence on the model \mathbf{m} may be expressed as

$$[13] \quad \mathbf{d} = \mathbf{F}[\mathbf{m}]$$

Since the dependence between data and model is linear in this study, the mathematical relationship between \mathbf{m} and \mathbf{d} may be expressed by the $M \times N$ matrix \mathbf{G} , such that

$$[14] \quad \mathbf{d} = \mathbf{G}\mathbf{m}$$

The misfit, X^2 in eq. [12], can then be written as

$$[15] \quad X^2 = \|\mathbf{W}\mathbf{d} - \mathbf{W}\mathbf{G}\mathbf{m}\|^2$$

where \mathbf{W} is the diagonal $M \times M$ matrix containing the uncertainties σ_j associated with each datum

$$[16] \quad \mathbf{W} = \text{diag}[1/\sigma_1, 1/\sigma_2, \dots, 1/\sigma_M]$$

The relative uncertainty, σ_j , is determined through the calculation of the sample standard deviation of the geodynamic predictions (for a given viscosity and velocity–density scaling profile) based on the seismic velocity heterogeneity in two tomography models, namely that of Grand (2002) and Ekström and Dziewonski (1998). We estimate the relative ability of the two models to predict similar values at given locations. The problem then reduces to finding the model \mathbf{m} , which possesses the smallest roughness possible, while X^2 achieves a statistically acceptable value. The roughness of the velocity–density scaling profiles is quantified by its first derivative in the inversions carried out here. Second-derivative regularization yields very similar results, provided the amplitude of the roughness weighting term is appropriately reduced. Further details concerning the roughness regularization scheme may be found in Constable et al. (1987).

Thermochemical structure of the continental tectosphere

Since shear-wave velocities alone cannot distinguish chemical heterogeneities in the tectosphere, it is necessary to combine the seismic results with geodynamic constraints on the density structure. We formulate our analysis in terms of the chemical heterogeneity resulting from partial melting of fertile mantle peridotite (Jordan 1979). The chemical heterogeneity is parameterized in terms of anomalies in iron content and garnet content, where the latter is treated as a proxy for variations in aluminum oxide.

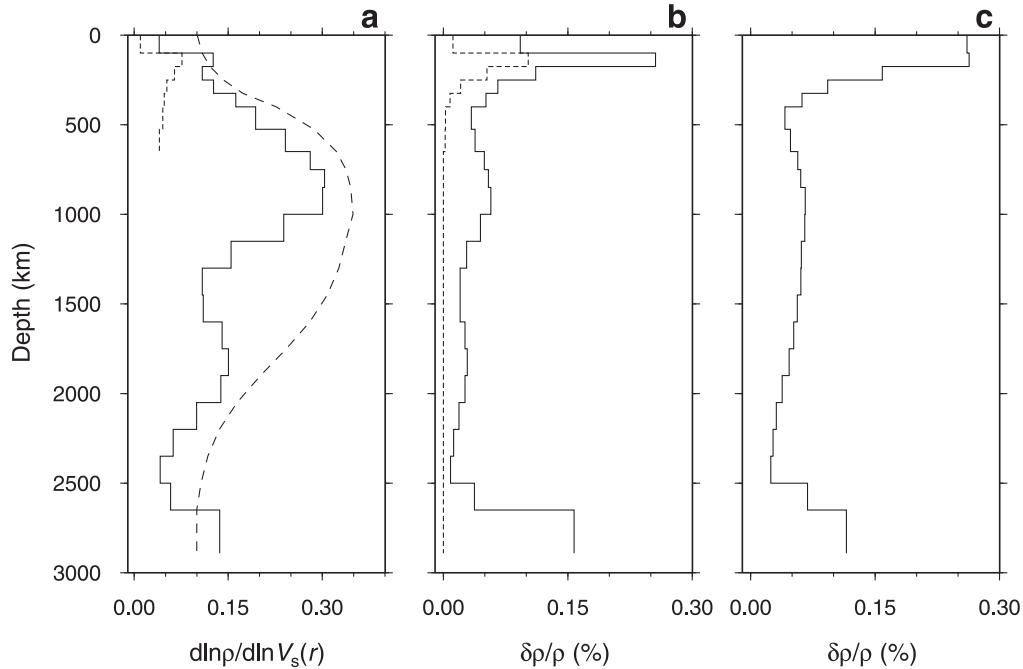
On the basis of estimates of the impact of temperature and compositional variations on seismic shear-wave velocity (see Appendix B), we estimate that the effect of basalt depletion on V_s will be substantially smaller than that due to temperature (see also Röhm et al. 2000), whereas the effect on ρ will be much larger. We note that basalt depletion in the tectosphere results in the simultaneous variation in its iron and garnet content (Jordan 1979). Therefore, to determine the extent of chemical depletion in the tectosphere, one must look to the density perturbations in the mantle, derived from the velocity–density scaling factors inferred from the inversions of geodynamic data.

Results

Velocity-to-density conversion

If V_s anomalies in the mantle resulted only from temperature perturbations, then there should be no difference between $(d \ln \rho/d \ln V_s)_{sh}$ and $(d \ln \rho/d \ln V_s)_{th}$. However, the

Fig. 4. Geodynamic inferences of the density structure in the Earth's mantle. (a) The long-dashed line represents the $d \ln \rho/d \ln V_s$ (velocity–density) scaling coefficient originally estimated by Karato (1993) on the basis of mineral physics data and subsequently modified on the basis of geodynamic data (Forte and Woodward 1997), where all heterogeneity is assumed to be thermal in origin. The short-dashed line represents $(d \ln \rho/d \ln V_s)_{sh}$, obtained through inversions of the geodynamic data (Table 1, inferred for the tectosphere seismic anomalies in the model of Grand (2002)). The solid line represents $(d \ln \rho/d \ln V_s)_{th}$ inferred for the seismic anomalies outside the tectosphere in the model of Grand (2002). (b) The root-mean-square (RMS) amplitude of the density perturbations, as a function of depth. The short-dashed and solid lines represent the rms amplitude of the density anomalies derived from the model of Grand (2002) in the tectosphere ($\delta\rho/\rho)_{sh}$ and outside the tectosphere ($\delta\rho/\rho)_{th}$, respectively. (c) The RMS amplitude of the density perturbations as a function of depth, derived from the mineral physics estimate of $d \ln \rho/d \ln V_s$ (long-dashed line in (a)).



effect of lower seismic attenuation in the tectosphere resulting from colder temperatures (Jordan 1981) implies $(d \ln \rho/d \ln V_s)_{sh} > (d \ln \rho/d \ln V_s)_{th}$ (Karato 1993). In contrast, the Occam inversions reveal that $(d \ln \rho/d \ln V_s)_{sh} < (d \ln \rho/d \ln V_s)_{th}$ (Fig. 4a), which implies that the density anomalies in the tectosphere do not result solely from temperature variations, suggesting the presence of chemical heterogeneity in the tectosphere. For the shield heterogeneity, we find that the minimum values of $(d \ln \rho/d \ln V_s)_{sh}$ occur in the upper 200 km of the mantle. We impose the 670 km boundary as the maximum depth to which cratons are explicitly identified, assuming that only “thermal” mantle persists below that depth. For the majority of the mantle in which thermal effects are assumed to dominate, the $(d \ln \rho/d \ln V_s)_{th}$ scaling peaks at ~ 800 km depth and diminish down to ~ 2500 km depth (Fig. 4a).

The density perturbations in the tectosphere, $(\delta\rho/\rho)_{sh} = (d \ln \rho/d \ln V_s)_{sh} (\delta V_s)_{sh}$, have a peak amplitude at ~ 150 km depth, with negligible amplitude below 250 km (Fig. 4b). We have not imposed convergence of $(d \ln \rho/d \ln V_s)_{sh}$ and $(d \ln \rho/d \ln V_s)_{th}$ below 670 km depth since $(\delta\rho/\rho)_{sh}$ is negligibly small at these depths. The density perturbations we obtained on the basis of the scaling of Karato (1993) are summarized in Fig. 4c. The most significant differences in $(\delta\rho/\rho)_{sh}$ predicted on the basis of the geodynamic constraints and that calculated from independent mineral physics con-

straints occurs at the top of the mantle (Figs. 4b, 4c). This is not surprising since we find the presence of significant chemical heterogeneity in this region, while Karato (1993) accounts only for the thermally generated heterogeneity.

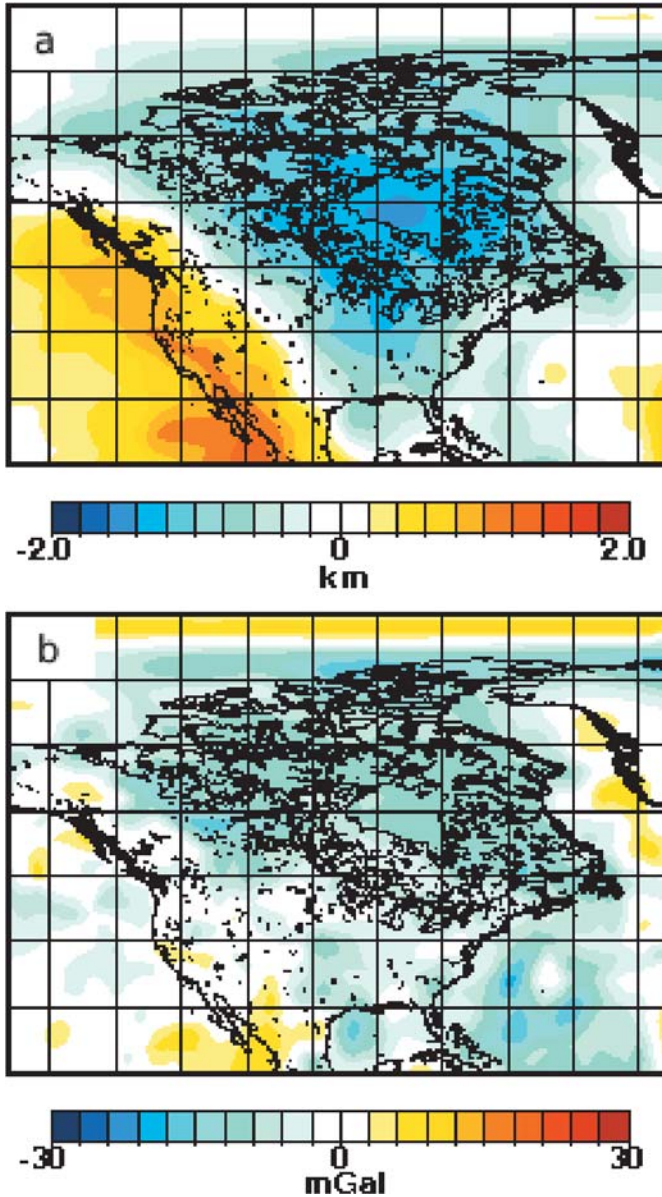
The mantle signal in the geodynamic data

Surface topography

The dynamic surface topography estimated on the basis of the LITH5.0 crustal correction is shown in Fig. 2c, and it is determined by subtracting the isostatic topography (Fig. 2b) and the post-glacial rebound contribution from the observed surface topography (Fig. 2a). Positive, or uplifted, dynamic topography is seen in the western Cordillera, in agreement with the high estimated mantle heat flux in this region (Hyndman and Lewis 1999). In general, however, the trend of depressed continental and elevated oceanic regions is evident. An annular region of approximately zero dynamic topography in the centre of the craton suggests that the isopycnic (neutral buoyancy) hypothesis (Jordan 1975) may be locally valid in the underlying continental lithosphere.

The dynamic topography predicted on the basis of a mantle viscosity and density structure inferred in a previous global study (Forte and Mitrovica 2001), assuming purely thermal buoyancy, is characterized by depressed continents and elevated oceans; however, the predicted depression of the North Ameri-

Fig. 5. (a) The dynamic surface topography predicted on the basis of the mantle viscosity and density structure (Fig. 3; Fig. 4b) inferred on the basis of the tomography model of Grand (2002). (b) The dynamic free-air gravity anomalies predicted on the basis of the mantle viscosity and density structure (Fig. 3; Fig. 4b) inferred on the basis of the tomography model of Grand (2002).



can continent is much greater than observed here in Fig. 2c. This suggests that composition plays an important role in determining the dynamic topography in the continents.

Free-air gravity anomalies

The dynamic free-air gravity signal is determined through the removal of the isostatic signal (Fig. 2e) and the post-glacial rebound contribution from the observed signal (Fig. 2d). The result is shown in Fig. 2f, where we note a clear depression of the residual gravity field (negative anomalies) centred in the Canadian craton, in the Hudson Bay region. This gravitational depression implies that the deeper portions of the North American lithospheric mantle must have a residual

negative buoyancy (i.e., characterized by positive density perturbations). These regional free-air gravity anomalies, therefore, provide buoyancy constraints that are independent and complementary to the dynamic topography constraints (Fig. 2c). The latter instead suggest that conditions in the shallow sub-continental mantle may be closer to that of neutral buoyancy.

Predicted geodynamic data sets

The regional (North American) dynamic surface topography and free-air gravity anomalies predicted on the basis of the new $d \ln \rho / d \ln V_s$ inferences are illustrated in Figs. 5a and 5b, respectively. A quantitative summary of the regional and global fits to the convection data achieved on the basis of the new $d \ln \rho / d \ln V_s$ inferences is provided in Table 1.

Thermochemical structure of the continental tectosphere

We use two estimates of chemical heterogeneity, one based on our internally consistent inferences of $d \ln \rho / d \ln V_s$ and the other based on independent mineral physics constraints. The chemical heterogeneity inferred on the basis of both approaches suggests greater iron and garnet depletion in the upper portion of the tectosphere, with a maximum depletion at ~ 150 km depth (Fig. 6). Below 250 km depth, the chemical heterogeneity diminishes rapidly, thereby delineating the base of the CBL below the North America, in agreement with the base of the CBL found in a recent global study (Forte and Perry 2000).

The reference molar ratio of iron ($R = X_{\text{Fe}} / (X_{\text{Fe}} + X_{\text{Mg}})$) for a pyrolytic mantle is 11% (Jackson 1998). Our inferred values of δR (Fig. 6) are perturbations relative to this reference value. These inferences of δR are determined on the basis of expression (eq. [B11]) in Appendix B, and they require a value of $(d \ln V_s / d \ln \rho)_{\text{th}}$ that describes the temperature sensitivity of V_s and ρ in the tectosphere. If we assume that seismic attenuation is negligible in the tectosphere, we can use independent mineral physics constraints on the anharmonic thermal conversion factors, such that $(d \ln V_s / d \ln \rho)_{\text{th}} \simeq 4$ in the upper mantle (Karato 1993). On the basis of this mineral physics estimate, the maximum inferred iron depletion is $\delta R = -0.022$ at ~ 150 km depth (Fig. 6), suggesting at least 20% fractionation of basalt in the tectosphere beneath North America (see table 6 in Jordan (1979)). If we instead employed our geodynamic inference for $(d \ln V_s / d \ln \rho)_{\text{th}}$, we find the maximum $\delta R = -0.004$ at the same depth. One possible problem with the latter estimate is the possible effect of partial melting or strong shear-velocity attenuation in the shallow thermal mantle, which would render the geodynamically inferred $(d \ln V_s / d \ln \rho)_{\text{th}}$ inappropriate in the context of the tectosphere. In comparison to a global study (Forte and Perry 2000), the two independently calculated depletion profiles (Fig. 6) show much more similarity, owing to the fact that we sample a smaller (continental) area, thus limiting the possibility of finding areas of widespread partial melting or strong attenuation globally distributed amongst different oceanic areas.

The spatial distribution of iron depletion, and the corresponding thermal anomalies at a depth of 150 km in the mantle, are represented in Fig. 7. The maximum temperature perturbations occur at ~ 150 km depth, corresponding to the depth of maximum iron depletion. The regions of maximum

Table 1. Fits to global and North American convection data.

3-D mantle*	Free-air gravity [†]		Plate divergence [‡]	Surface topography [§]		Excess CMB ellipticity
	Global [$\ell = 2-32$]	N. Amer.	[$\ell = 1-32$]	[$\ell = 1-32$]	N. Amer.	
Grand [#]	26%	36%	60%	26%	-52%	-0.50 km
Grand [¶]	27%	29%	59%	50%	57%	-0.52 jn

Note: All fits are quantified in terms of percent variance reduction (e.g., Forte 2007, p. 834). For the global fits all data and predictions are filtered to maximum spherical harmonic degree 32 and for the North American (N. Amer.) fits all fields are filtered to maximum harmonic degree 128.

*Mantle flow predictions of geodynamic observables use the tomography model of Grand (2002) in this study.

[†]The observed free-air gravity anomalies calculated with the nonhydrostatic gravitational potential derived from satellite data. The free-air gravity anomalies in North America are derived from the satellite data of the EGM96 model (Lemoine et al. 1996), while the global free-air gravity anomalies are derived from the satellite data of the GEM-T2 model (Marsh et al. 1990).

[‡]Plate motion data are represented in terms of the horizontal divergence of the plate velocities given by the NUVEL-1 model (DeMets et al. 1990).

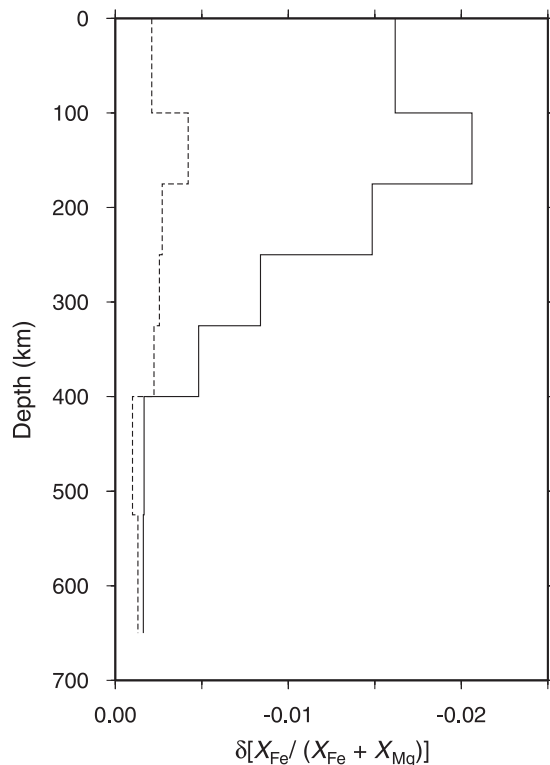
[§]The dynamic surface topography in North America is obtained from the observed surface topography after removal of the isostatic crustal contribution (Figs. 2a–2c), while the global dynamic surface topography is obtained after an isostatic crustal reduction of the observed topography using Mooney et al. (1998).

^{||}The recent inference of excess dynamic core–mantle boundary (CMB) ellipticity Mathews et al. (2002) suggests a value of about 0.4 km.

[#]The density perturbations in the mantle-flow models are derived from the shear-wave velocity anomalies using $d \ln \rho/d \ln V_s$ (long-dashed curve, Fig. 4a), which is based on an estimate originally obtained by Karato (1993).

[¶]The density perturbations are derived on the basis of the associated $d \ln \rho/d \ln V_s$ profiles (solid and short-dashed curves, Fig. 4a) inferred in inversions of the convection data. The $d \ln \rho/d \ln V_s$ conversion inferred for the North American tectosphere (short-dashed curve, Fig. 4a) is only applied to this continental root in the calculation of global convection observables.

Fig. 6. Iron depletion δR in the tectosphere, where R is the reference molar ratio of iron ($= X_{\text{Fe}}/(X_{\text{Fe}} + X_{\text{Mg}})$). The solid line represents the estimate of δR , obtained with independent mineral physics data (Karato 1993), inferred from the model of Grand (2002). The dashed line represents the internally consistent estimate of tectosphere heterogeneity, inferred on the basis of an Occam inversion of the convection data, expressed in terms of peak values of the perturbation to the iron molar ratio R in each layer of the tomography model of Grand (2002).



iron depletion are found beneath the Canadian Shield, whereas the Phanerozoic Cordillera exhibits a much lower degree of depletion. The regions of maximum chemical depletion are correlated to regions of coldest temperatures below the Precambrian Shield of North America.

Similar results are found in petrological and geochemical analyses of mantle xenoliths from the Canadian Shield. Gaul et al. (2000) address the Mg# in mantle profiles, where $\text{Mg\#} = 1 - R = X_{\text{Mg}}/(X_{\text{Fe}} + X_{\text{Mg}})$, derived directly from xenolith and xenocryst data for kimberlites worldwide, including the Slave Province. They concluded that the iron content in olivine is smallest toward the top of the sections, consistent with the higher degrees of partial melting at shallow depth predicted by models of melting during adiabatic decompression. In the Slave Province in particular, they found a distinct stratification of the lithospheric mantle, with a highly depleted upper layer and a lower layer of less depleted peridotitic mantle, the two layers separated by a boundary at a depth ~ 50 km. Peridotites from the Canadian Shield region are found to contain much higher Mg# suggesting that they are more refractory than the lithospheric mantle in the Phanerozoic Cordillera (Schmidberger and Francis 1999). Griffin et al. (2004) present a detailed chemical analysis of the North American lithospheric mantle using empirical xenolith data with detailed profiles of olivine Mg#.

The coldest temperatures are found in the centre of the North American craton, and they become less cold toward its edges (Fig. 7b). Seismic and magnetotelluric studies place the lithosphere–asthenosphere transition at ~ 200 –250 and 195 km, respectively (Jones and Ferguson 1997; Bostock 1997). Pressure–temperature (P – T) estimates from xenoliths suggest minimum lithospheric thicknesses of ~ 180 –190 km (MacKenzie and Canil 1999; Kopylova et al. 1998; Boyd and Canil 1997) in the centre of the Slave Province. The occurrence of an inflection in the P – T array of a mantle xenolith suite from the Canadian Arctic at 140 km depth reported by Schmidberger and Francis (1999) may suggest that the transition from the base of the lithosphere shallows from the centre of the Slave craton to its margin beneath Somerset Island. Boyd (1987) reports simi-

Fig. 7. Chemical and thermal structure of the mantle beneath North America at 150 km depth. (a) Iron depletion δR in the tectosphere inferred on the basis of the Grand (2002) shear-velocity heterogeneity model and employing independent mineral physics data to estimate the thermal properties of the tectosphere. (b) Lateral temperature variations inferred on the basis of the Grand (2002) model and using, as in (a), independent mineral physics constraints on the tectosphere's thermal properties.

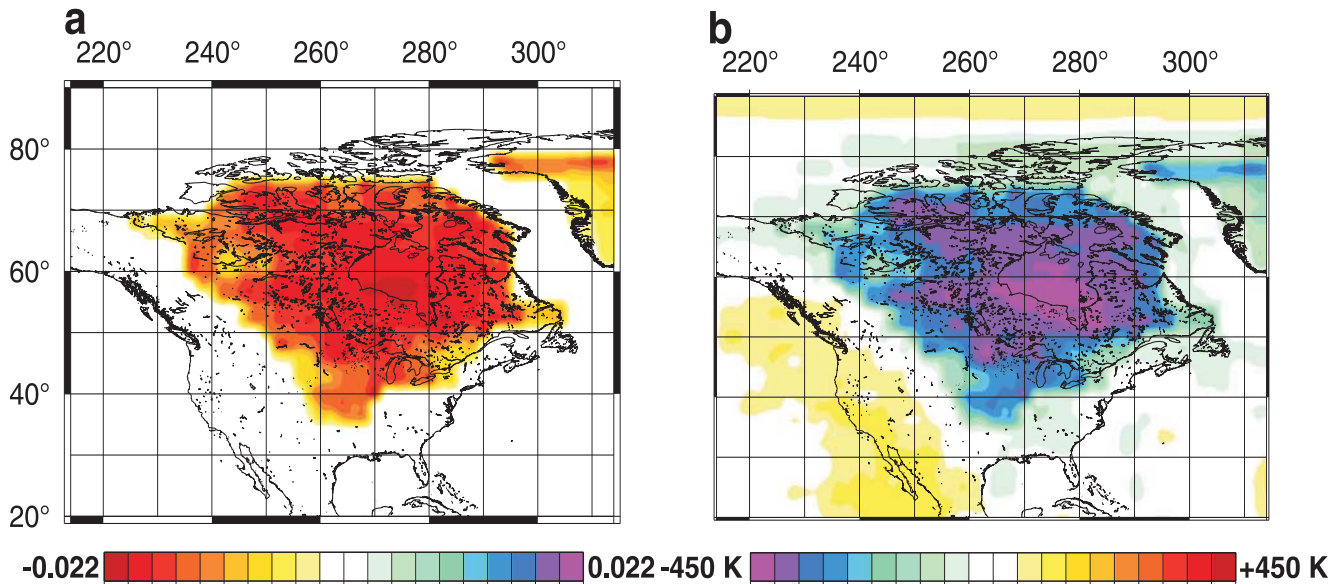
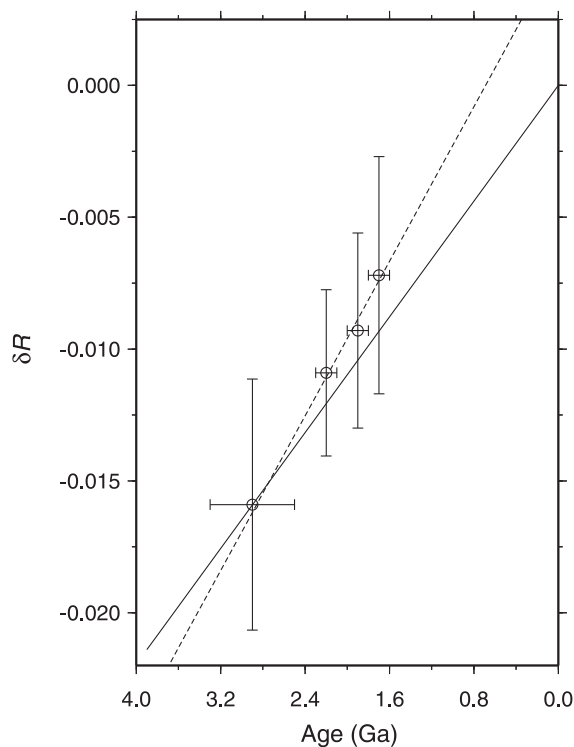


Fig. 8. Iron depletion, δR , as a function of tectonothermal age of crustal rocks, where variations in δR are based on and the tectonothermal age range of crustal groups according to Hoffman (1989). The dashed-line marks the line of best fit. The solid line is one possible solution within the bounds of the crustal age groups and the variation in δR and shows that, at time $t = 0$, the mantle is fertile and undepleted in its iron components.



lar shallowing of the lithosphere–asthenosphere transition for the Kaapvaal craton from its centre (200 km) to its margins (~ 140 km).

Uncertainties in chemical composition and temperature

The uncertainties inherent in our predictions of Mg# (or equivalent Fe#) deserve some scrutiny. They can be estimated on the basis of an assumed 20% uncertainty in the crust-corrected (dynamic) topography. This error estimate follows from the analysis of Pari (2001), who considered the uncertainties associated with predictions of dynamic topography resulting from uncertainties in both the crustal layer thickness and P -velocity-to-density systematics of Christensen and Mooney (1995). Pari (2001) noted that the errors in the conversion of P -velocity to density provide the dominant contributions to the total error since the densities are multiplied by large values of the continental crust thickness in the isostatic topography calculation.

A 20% error in the observed dynamic topography translates to a significant uncertainty in our predictions of Fe depletion and corresponding Mg# in the tectosphere. It should be noted that the (comparatively small) uncertainties in the observed dynamic free-air gravity anomalies are not considered in this instance. These depend on the uncertainty in the isostatic free-air gravity anomaly, which contributes only a small fraction to the observed free-air gravity anomaly. The uncertainty in the predicted temperature perturbation at 150 km depth is ~ 100 K, compared with a background anomaly of about 500 K at this depth (Fig. 7).

Iron depletion in cratonic mantle

We examined the secular trend in the iron composition of xenolith suites from North America. For this purpose, we fo-

cused on the four tectonothermal crustal age distributions given by Hoffman (1989): one Archean (3.3–2.5 Ga) and three Early Proterozoic (2.5–1.6 Ga). The exclusion of the oldest Archean rocks is valid since our spatial resolution of the δR values is not less than $2^\circ \times 2^\circ$, and the point occurrences of these old Archean rocks are very localized. The computed δR values of the sub-continental mantle rock are assigned the tectonothermal age of the corresponding overlying crust.

To estimate the amount of iron depletion in the tectosphere, δR , for crustal age t , one must account for uncertainties in both crustal age and δR . We adopt a measure of misfit that incorporates both the δR estimates and the tectonothermal crust age. A model of the δR –age relationship is generated by computing infinitely many random points that are valid within the range of δR values for a given crustal age. We seek a linear regression line consistent with the uncertainties that intersects the point $\delta R = 0$ at time $t = 0$. We find that such a line exists, supporting the hypothesis that the mantle is fertile and undepleted in its iron constituents at time $t = 0$ (Fig. 8).

The trend of increasing iron depletion with the age of SCLM lithosphere probably suggests that the petrogenetic processes creating lithospheric mantle have changed with time. Petrological analyses of xenolith and xenocryst samples worldwide suggest that the roots of most Proterozoic shields probably consist of refertilized Archean SCLM and the juvenile SCLM beneath Proterozoic and Phanerozoic mobile belts reflects only moderate depletion of primitive mantle compositions (Griffin et al. 2009). This secular evolution in SCLM composition, related to tectonothermal age of the overlying crust, is evident in the petrological analyses of garnet xenocrysts from O'Reilly and Griffin (2006). These studies are consistent with the predictions of Schmidberger and Francis (1999), who suggest that the Mg# of Archean SCLM beneath the Canadian Shield is higher than that of SCLM beneath the Phanerozoic Canadian Cordillera at the western margin of the shield. A similar trend is recorded by Poudjom-Djomani et al. (2001), where Mg# was shown to decrease secularly in mantle-derived peridotite xenoliths and garnet-xenocryst suites from Archean (highest Mg#) to Phanerozoic (lowest Mg#).

Discussion

Effect of viscosity variations and boundary conditions

The geodynamic inversions for optimal $d \ln \rho / d \ln V_s$ conversion factors in the North American “shield” mantle and the exterior “thermal” mantle (Fig. 4) yield similar fits to the global-scale and regional-scale (i.e., North American) data sets (Table 1); however, the fit to the latter is slightly better. This would indirectly suggest that the effect of lateral viscosity variations are relatively small in the North American SCLM.

To better understand why the joint modelling of global and regional convection-related data does not seem to require an explicit treatment of lateral viscosity variations, we refer to the work of Forte and Peltier (1994). Their quasi-analytic treatment of buoyancy-induced flow in the presence of large-scale lateral viscosity variations suggests that the predicted surface topography and geoid anomalies are weakly affected, provided the same horizontally averaged profile of viscosity is used. Forte and Mitrovia (2001) and Moucha et

al. (2007) calculated the large-scale viscosity heterogeneity expected on the basis of temperature anomalies derived from global seismic tomography, and they also showed the resulting impact on global convection data is in the order of 10% to 20%, less than current uncertainties in the global tomography models. An explicit calculation of the relatively minor effect of lateral viscosity variations on predicted dynamic topography in North America is presented in Forte et al. (2010). The lateral viscosity variations which may be predicted on the basis of our inferred temperature anomalies (Fig. 7) are on a similarly large scale as in the recent study by Forte et al. (2010), and this is why we should expect a similarly small effect.

We test the importance of lateral viscosity variations by considering the differences between regional- and global-scale inferences of mantle viscosity derived from inversions of different types of geodynamic data. We consider the two viscosity profiles presented in Fig. 3: the first being the dotted curve, derived by simultaneously inverting global convection and post-glacial rebound data (Mitrovia and Forte 2002), and the second being the solid curve, the convection viscosity profile. The dynamic surface topography predicted with the joint rebound–convection viscosity profile differs from the prediction obtained with the pure convection profile by only 14%, despite the large difference between the two viscosity profiles, especially in the upper mantle. This result further reinforces our conclusion that large-scale lateral viscosity variations have a relatively small impact on the geodynamic surface predictions.

The impact of rigid tectonic plates, whose motions are coupled to the underlying buoyancy-driven mantle, is as important as the effect of lateral viscosity variations. Indeed, it may be argued that the plates are a manifestation of lateral heterogeneity in rheological behaviour (e.g., Tackley 2000). According to the treatment of rigid plates developed by Forte and Peltier (1991, 1994), the plates enforce a partitioning of the internal density anomalies into two components: (i) one that is spatially correlated with the global plate boundary geometry and is thus able to drive observable plate motions (these density anomalies are, therefore, modelled with a free-slip boundary condition); and (ii) one that is spatially uncorrelated (effectively “orthogonal”) to the plate boundaries and, therefore, cannot produce observable plate motions. The latter density anomalies must, therefore, be modelled with a no-slip condition at the surface. Density anomalies that are significantly displaced relative to the location of the plate boundaries can, therefore, produce little or no horizontal movement of the overlying plates, as shown in Forte (2007). These density anomalies effectively see a local rigid surface boundary condition, and this is the case for the regional density anomalies below North America.

Perry et al. (2003) compared the regional dynamic topography predicted with a (global) no-slip condition and the regional topography predicted with a global flow model which incorporates moving tectonic plates involving both free-slip and no-slip conditions. The relative difference between the two predictions is only 5%. Evidently, the assumption of a rigid surface boundary for the regional modelling of flow below North America is a robust and accurate approximation and it represents the primary, effectively “rheological,” control on the underlying flow dynamics.

Geodynamic inversions

The dynamic topography predicted on the basis of mineral physics data, which assume that mantle heterogeneity is mainly thermal in origin, provides a rather poor fit to the data (Table). The assumption of a dominant thermal origin for the seismically imaged heterogeneity is evidently an inaccurate approximation for the continental tectosphere, where colder temperatures coexist with chemically depleted mantle material. This being said, to interpret compositional heterogeneity in SCLM, joint seismic–geodynamic inversions of the density structure are necessary, since shear-wave velocity anomalies alone are weakly affected by chemical variations within the SCLM. In oceanic regions, a purely thermally derived scaling is more appropriate since the sub-oceanic mantle lacks the chemical heterogeneity present in its sub-continental counterpart.

As noted earlier in the text, the constraints on tectosphere density structure provided by topography data differ from the free-air gravity constraints. To underline this point, we note that an analysis of free-air gravity anomalies over North America by Pari and Peltier (2000) conclude that the rebound process accounts for only 10% of the observed free-air gravity low over Hudson Bay. They suggest that the main source of the anomaly arises from mantle convection (e.g., Peltier et al. 1992). They deduce that, at very long wavelengths, the nonhydrostatic free-air gravity field favours the existence of high-density sub-continental mantle and suggest (following Forte et al. (1993)) that it is through the downward stresses exerted on the Earth's surface by these anomalous high-density masses that depressions in the dynamic topography of continental regions are sustained over time relative to oceanic regions. To obtain these results they use a priori estimates of $(d \ln \rho / d \ln V_s)_{sh}$ above 175 km depth, which assume either positive or negative values, implying negative or positive buoyancy for fast sub-continental anomalies, respectively.

Through the joint inversion of the full suite of convection data (in particular the combined topography and gravity anomalies), we find $(d \ln \rho / d \ln V_s)_{sh}$ varies from 0.01 at the surface to a peak value of 0.08 at ~ 150 km depth, decreasing to ~ 0.05 at the base of the tectosphere (Fig. 4a). Pari (2001) finds that a best fit to the long-wavelength dynamic surface topography signal is obtained when $(d \ln \rho / d \ln V_s)_{th} = 0.15$ at depths >175 km, a result predicted independently through our inversions of the velocity–density conversion factors. The density structure of the sub-cratonic mantle has a significant impact on both the predicted dynamic surface topography and free-air gravity anomalies, and thus a joint inversion for $(d \ln \rho / d \ln V_s)_{sh}$ is essential in determining the dynamical processes effecting the sub-continental mantle convective flow. To further emphasise this point, we note in Table 1 that a purely thermally derived velocity–density scaling (e.g., Karato 1993) seems to provide a better fit to the local North America gravity data, but it yields a dynamic topography prediction that is clearly incorrect.

Conclusions

Several studies have attempted to evaluate the effect of melt depletion on garnet peridotite buoyancy in the mantle (e.g., O'Hara 1975; Oxburgh and Parmentier 1977; Jordan

1979). O'Hara (1975) suggests that partial melting in the upper mantle generally decreases Fe/(Fe + Mg) in the mantle rock residuum and depletes the dense garnet component, and that residual material should be about 2.5% less dense than undepleted mantle for 20% partial melting. These results were supported by experimental studies on two natural peridotites (Boyd and Callister 1976). Oxburgh and Parmentier (1977) predicted that 25% partial melting beneath an oceanic ridge will result in a decrease in density of $\sim 1.9\%$ for the mantle source. Our results indicate that the North American tectosphere is $\sim 2.2\%$ more depleted in iron at 150 km depth than the average mantle. These inferences of iron depletion for the North American sub-continental lithospheric mantle suggest that repeated episodes of partial melting of this region are required over its very long tectonic history. These repeated episodes of partial melting would then lead to the creation of long-lived, chemically buoyant cratonic roots.

It is important to note that our estimated iron depletion profile shows maximum depletion at 150 km. Therefore, our estimate of $\sim 2.2\%$ more iron depletion at 150 km depth compared with the average mantle represents an upper bound estimate of total iron depletion in Archean SCLM. Almost all depth profiles of Mg# (olivine) obtained from petrological analyses of garnet xenoliths and xenocrysts suggest an increase in Fe content with depth, associated with refertilization by asthenospheric fluids. In xenolith and xenocryst data sets worldwide (e.g., Slave Province and Kaapvaal), this decrease in depletion tends to occur below ~ 150 km (O'Reilly and Griffin 2006; Griffin et al. 2009), marking the boundary between an ultradepleted upper layer and a refertilized lower layer. In the Slave Province, this same “layering” at 150 km depth is evident from teleseismic analyses (Snyder et al. 2004). These petrological and seismic results correlate very well with our predicted depth of maximum iron depletion around 150 km depth.

Considering the contributions to density from both iron depletion and temperature in the North American tectosphere, we find a total positive density anomaly of $\sim 0.25\%$ compared with that of the surrounding mantle. This suggests a slightly heavy tectosphere, which is consistent with the negative free-air gravity anomaly over the craton. One possible explanation for our prediction of lesser Fe depletion relative to isopycnic equilibrium is the presence of denser lithologies (e.g., eclogite or Fe-rich peridotites) that contribute to the average density of the tectosphere, but remain largely unsampled (Lee 2003). Eclogites are generally associated with zones of intense metasomatism in adjacent peridotites, and reflect the introduction of Fe among other heavy elements into the base of the depleted SCLM. On the other hand, most of the published Mg# (olivine) profiles based on xenolith and xenocryst petrological analyses, show a general increase in Fe with depth reflecting refertilization from asthenospheric fluids infiltrating upwards from the lithosphere–asthenosphere boundary. It seems unlikely that there could be enough eclogite to produce this effect as only $<5\%$ is likely for any given mantle section (e.g., Griffin and O'Reilly 2007).

Future perspectives

On the basis of more recent work involving joint inversions of global seismic and geodynamic data sets (Simmons

et al. 2006), we will be revisiting the compositional and thermal mapping of the tectosphere. The most recent joint seismic–geodynamic inversions (Simmons et al. 2007, 2009) suggest higher degrees of sub-continental depletion in the lithosphere and higher local magnesium numbers than previously estimated. The methodology presented in this review will be used to carry out future studies of the lithospheric thermochemical and density structure using these recent high-resolution tomography models. Heat-flow data sets will also be incorporated into our current inversion scheme, thereby providing another independent and fundamentally important constraint on the thermal component of lithospheric density.

Acknowledgements

We are grateful for the significant contributions provided by D.W.S. Eaton in the development of the LITH5.0 crustal model. We are also grateful to J.X. Mitrovica for providing the glacial isostatic adjustment corrections for the Hudson Bay region. We acknowledge thorough reviews and comments by Suzanne O'Reilly, an anonymous reviewer, and the Associate Editor, Ron Clowes.

References

- Begg, G.C., Griffin, W.L., Natapov, L.M., O'Reilly, S.Y., Grand, S.P., O'Neill, C.J., et al. 2009. The lithospheric architecture of Africa: Seismic tomography, mantle petrology, and tectonic evolution. *Geosphere*, **5**. doi:10.1130/GES00179.1.
- Bostock, M.G. 1997. Anisotropic upper-mantle stratigraphy and architecture of the slave craton. *Nature*, **390**: 392–395.
- Boyd, F.R. 1987. High- and low-temperature garnet peridotite xenoliths and their possible relation to the lithosphere-asthenosphere boundary beneath southern Africa. *In* *Mantle xenoliths*. Edited by P.H. Nixon. Wiley, New York, N.Y., pp. 402–412.
- Boyd, F.R., and Callister, R.H. 1976. Densities of fertile and sterile garnet peridotites. *Geophysical Research Letters*, **3**: 509–512.
- Boyd, F.R., and Canil, D. 1997. Peridotite xenoliths from the Slave craton, Northwest Territories. *In* 7th annual Conference. Edited by V.M. Goldschmidt. Lunar and Planetary Institute, Houston, Tex., pp. 34–35.
- Boyd, F.R., Gurney, J.J., and Richardson, S.H. 1985. Evidence for a 150–200 km thick Archaean lithosphere from diamond inclusion thermobarometry. *Nature*, **315**: 387–398.
- Christensen, N.I., and Mooney, W.D. 1995. Seismic velocity structure and composition of the continental crust: A global view. *Journal of Geophysical Research*, **100**: 9761–9788.
- Clowes, R.M., Cook, F.A., Green, A.G., Keen, C.E., Ludden, J.N., Percival, J.A., Quinlan, G.M., and West, G.F. 1992. Lithoprobe — new perspectives on crustal evolution. *Canadian Journal of Earth Sciences*, **29**: 1831–1864.
- Constable, S.C., Parker, R.L., and Constable, C.G. 1987. Occam's inversion: A practical algorithm for generating smooth models from electromagnetic sounding data. *Geophysics*, **52**: 289–300.
- Corrieu, V., Ricard, Y., and Froidevaux, C. 1994. Converting mantle tomography into mass anomalies to predict the Earth's radial viscosity. *Physics of the Earth and Planetary Interiors*, **84**: 3–13.
- DeMets, C.R., Gordon, R.G., Argus, D.F., and Stein, S. 1990. Current plate motions. *Geophysical Journal International*, **101**: 425–478.
- Deschamps, F., Trampert, J., and Snieder, R. 2002. Anomalies of temperature and iron in the uppermost mantle inferred from gravity data and tomographic models. *Physics of the Earth and Planetary Interiors*, **129**: 245–264.
- Doin, M.P., Fleitout, L., and McKenzie, D. 1996. Geoid anomalies and the structure of continental and oceanic lithospheres. *Journal of Geophysical Research*, **101**: 16 119–16 135.
- Dziewonski, A.M., and Anderson, D.L. 1981. Preliminary reference Earth model. *Physics of the Earth and Planetary Interiors*, **25**: 297–356.
- Ekström, G., and Dziewonski, A.M. 1998. The unique anisotropy of the Pacific upper mantle. *Nature*, **394**: 168–172.
- Finnerty, A.A., and Boyd, F.R. 1987. Thermobarometry for garnet peridotites: basis for the determination of thermal and compositional structure of the upper mantle. *In* *Mantle xenoliths*. Edited by P.H. Nixon. Wiley, New York, N.Y., pp. 381–402.
- Fischer, K.M., and van der Hilst, R.D. 1999. A seismic look under the continents. *Science*, **285**: 1365–1366.
- Forte, A.M. 2000. Seismic–geodynamic constraints on mantle flow: Implications for layered convection, mantle viscosity, and seismic anisotropy in the deep mantle. *In* *Earth's Deep Interior: Mineral Physics and Tomography From the Atomic to the Global Scale*. Edited by S.I. Karato, A.M. Forte and R.C. Liebermann. American Geophysical Union (AGU) Monograph 117, Washington, D.C., pp. 3–36.
- Forte, A.M. 2007. Constraints on seismic models from other disciplines — Implications for mantle dynamics and composition. *In* *Treatise of geophysics*. Edited by A. Dziewonski and B. Romanowicz. Elsevier, Amsterdam, the Netherlands, Vol. 1, pp. 805–858.
- Forte, A.M., and Mitrovica, J.X. 2001. Deep-mantle high-viscosity flow and thermochemical structure inferred from seismic and geodynamic data. *Nature*, **410**: 1049–1056.
- Forte, A.M., and Peltier, W.R. 1987. Plate tectonics and aspherical Earth structure: The importance of poloidal-toroidal coupling. *Journal of Geophysical Research*, **92**: 3645–3679.
- Forte, A.M., and Peltier, W.R. 1991. Viscous models of global geophysical observables, 1. Forward problems. *Journal of Geophysical Research*, **96**: 20 131–20 159.
- Forte, A.M., and Peltier, W.R. 1994. The kinematics and dynamics of poloidal-toroidal coupling in mantle flow: The importance of surface plates and lateral viscosity variations. *Advances in Geophysics*, **36**: 1–119.
- Forte, A.M., and Perry, H.K.C. 2000. Geodynamic evidence for a chemically depleted continental tectosphere. *Science*, **290**: 1940–1944.
- Forte, A.M., and Woodward, R.L. 1997. Seismic–geodynamic constraints on three-dimensional structure, vertical flow, and heat transfer in the mantle. *Journal of Geophysical Research*, **102**: 17 981–17 994.
- Forte, A.M., Peltier, W.R., Dziewonski, A.M., and Woodward, R.L. 1993. Dynamic surface topography: A new interpretation based upon mantle flow models derived from seismic tomography. *Geophysical Research Letters*, **20**: 225–228.
- Forte, A.M., Woodward, R.L., and Dziewonski, A.M. 1994. Joint inversions of seismic and geodynamic data for models of three dimensional mantle heterogeneity. *Journal of Geophysical Research*, **99**: 21 857–21 877.
- Forte, A.M., Dziewonski, A.M., and O'Connell, R.J. 1995. Continent–ocean chemical heterogeneity in the mantle based on seismic tomography. *Science*, **268**: 386–388.
- Forte, A.M., Moucha, R., Simmons, N.A., Grand, S.P., and Mitrovica, J.X. 2010. Deep mantle contributions to the surface dynamics of the North American continent. *Tectonophysics*, **481**: 3–15. doi:10.1016/j.tecto.2009.06.010.
- Gaul, O., Griffin, W.L., O'Reilly, S.Y., and Pearson, N.J. 2000. Mapping olivine composition in the lithospheric mantle. *Earth and Planetary Science Letters*, **182**: 223–235.
- Godey, S., Deschamps, F., Trampert, J., and Snieder, R. 2004. Thermal and compositional anomalies beneath the North American continent. *Journal of Geophysical Research*, **109**: B01308. doi:10.1029/2002JB002263.

- Goes, S., Govers, R., and Vacher, P. 2000. Shallow mantle temperatures under Europe from *P* and *S* wave tomography. *Journal of Geophysical Research*, **105**: 11153–11169.
- Grand, S.P. 2002. Mantle shear-wave tomography and the fate of subducted slabs. *Philosophical Transactions of the Royal Society of London. Series A: Mathematical and Physical Sciences*, **360**: 2475–2491.
- Griffin, W.L., and O'Reilly, S.Y. 2007. Cratonic lithospheric mantle: Is anything subducted? *Episodes*, **1**: 43–53.
- Griffin, W.L., O'Reilly, S.Y., Doyle, B.J., Pearson, N.J., Kivi, K., Malkovet, V., Coopsmith, H., and Pokhilenko, N.V. 2004. Lithosphere Mapping beneath the North American Plate. *Earth and Planetary Science Letters*, **77**: 873–922.
- Griffin, W.L., O'Reilly, S.Y., Afonso, J.C., and Begg, G.C. 2009. The composition and evolution of lithospheric mantle: A re-evaluation and its tectonic implications. *Journal of Petrology*, **50**. doi:10.1093/petrology/egn033.
- Hager, B.H., and Richards, M.A. 1989. Long-wavelength variations in the Earth's geoid: physical models and dynamical implications. *Philosophical Transactions of the Royal Society of London. Series A: Mathematical and Physical Sciences*, **328**: 309–327.
- Herring, T.A., Mathews, P.M., and Buffett, B.A. 2002. Modelling of nutation–precession: Very long baseline interferometry. *Journal of Geophysical Research*, **107**(B4). doi:10.1029/2001JB000165.
- Hoffman, P.F. 1989. Precambrian geology and tectonic history of North America. *In The Geology of North America — An Overview. Edited by A.W. Bally and E.R. Palmer*, pp. 447–512. Boulder, CO: GSA.
- Hyndman, R.D., and Lewis, T.J. 1999. Geophysical consequences of the Cordillera-Craton thermal transition in southwestern Canada. *Tectonophysics*, **306**: 397–422.
- Jackson, I. 1998. Elasticity, composition and temperature of the Earth's lower mantle: A reappraisal. *Geophysical Journal International*, **134**: 291–311.
- Jaques, A.L. 1987. Diamond bearing lamproites from western Australia: Multiple tapping of old enriched lithosphere beneath Proterozoic mobile belts. *Terra Cognita*, **7**: 616.
- Jaupart, C., and Mareschal, J.-C. 1999. The thermal structure and thickness of continental roots. *Lithos*, **48**: 93–114.
- Jones, A.G., and Ferguson, I.J. 1997. Results from 1996 MT studies along SNORCLE profiles 1 and 1A. *In Slave – Northern Cordillera Lithospheric Evolution (SNORCLE) Transect and Cordilleran Tectonics Workshop meeting*, University of Calgary, Calgary, Alta. *Edited by F. Cook and P. Erdmer*. Lithoprobe Report 56, pp. 42–47.
- Jordan, T.H. 1975. The continental tectosphere. *Reviews of Geophysics and Space Physics*, **13**: 1–12.
- Jordan, T.H. 1978. Composition and development of the continental tectosphere. *Nature*, **274**: 544–548.
- Jordan, T.H. 1979. The mantle sample: Inclusions in kimberlites and other volcanics. *In Proceedings of the 2nd International Kimberlite Conference. Edited by F.R. Boyd and H. Meyer*. AGU, Washington, D.C., pp. 1–14.
- Jordan, T.H. 1981. Continents as a chemical boundary layer. *Philosophical Transactions of the Royal Society of London. Series A: Mathematical and Physical Sciences*, **301**: 359–373.
- Karato, S.I. 1993. The importance of anelasticity in the interpretation of seismic tomography. *Geophysical Research Letters*, **20**: 1623–1626.
- Kopylova, M.G., Russell, J.K., and Cookenboo, H. 1998. Upper-mantle stratigraphy of the Slave craton, Canada: insights into a new kimberlite province. *Geology*, **26**: 315–318.
- Lee, C.-T.A. 2003. Compositional variation of density and seismic velocities in natural peridotites at STP conditions: Implications for seismic imaging of compositional heterogeneities in the upper mantle. *Journal of Geophysical Research*, **108**(B9): 2441. doi:10.1029/2003JB002413.
- Lemoine, F.G., Kenyon, S.C., Factor, J.K., Trimmer, R.G., Pavlis, N.K., Chinn, D.S., et al. 1996. The development of the joint NASA GSFC and NIMA geopotential model EGM96. NASA Goddard Space Flight Center, Greenbelt, Md.
- Li, A., Fischer, K.M., Wysession, M.E., and Clarke, T.J. 1998. Mantle discontinuities and temperature under the North American continental keel. *Nature*, **395**: 160–163.
- MacKenzie, J.M., and Canil, D. 1999. Composition and thermal evolution of cratonic mantle beneath the central Archean Slave Province, NWT, Canada. *Contributions to Mineralogy and Petrology*, **134**: 313–324.
- Mareschal, J.-C., and Jaupart, C. 2006. Archean thermal regime and stabilization of the cratons. *In Archean geodynamic processes and environments. Edited by K. Benn, J.-C. Mareschal, and K.C. Condie*. AGU, Washington, D.C., Vol. 164, pp. 61–74.
- Mareschal, J.C., Jaupart, C., Gariépy, C., Cheng, L.Z., Guillou-Frotier, L., Bienfait, G., and Lapointe, R. 2000. Heat flow and deep thermal structure near the southeastern edge of the Canadian Shield. *Canadian Journal of Earth Sciences*, **37**: 399–414.
- Marsh, J.G., Lerch, F.J., Putney, B.H., Felsentreger, T.L., Sanchez, B.V., Klosko, S.M., et al. 1990. The GEM-T2 gravitational model. *Journal of Geophysical Research*, **95**: 22043–22071.
- Mathews, P.M., Hering, T.A., and Buffett, B.A. 2002. Modeling of nutation–precession: New nutation series for nonrigid Earth and insights into the Earth's interior. *Journal of Geophysical Research*, **107**. doi: 10.1029/2001JB000390
- Méglin, C., and Romanowicz, B. 2000. The three-dimensional shear velocity structure of the mantle from inversion of body, surface and higher-mode waveforms. *Geophysical Journal International*, **143**: 709–728.
- Mitrovica, J.X. 1997. Going halves over Hudson Bay. *Nature*, **390**: 444–447.
- Mitrovica, J.X., and Forte, A.M. 2002. On the radial profile of mantle viscosity. *In Glacial isostatic adjustment and the Earth system: sea-level, crustal deformation, gravity and rotation. Edited by J.X. Mitrovica and L.L.A. Vermeersen*. AGU, Washington, D.C., Geodynamics Research Series, Vol. 29.
- Mitrovica, J.X., and Forte, A.M. 2004. A new inference of mantle viscosity based upon joint inversion of convection and glacial isostatic adjustment data. *Earth and Planetary Science Letters*, **225**: 177–189.
- Mooney, W.D., Laske, G., and Masters, T.G. 1998. CRUST5.1: A global crustal model at 5° × 5°. *Journal of Geophysical Research*, **103**: 727–747.
- Moucha, R., Forte, A.M., Mitrovica, J.X., and Daradich, A. 2007. Lateral variations in mantle rheology: Implications for convection related surface observables and inferred viscosity models. *Geophysical Journal International*, **169**: 113–135.
- National Geophysical Data Center. 1988. Etopo-5, bathymetry/topography data. Data announcement 88-MGG-02; National Oceanic and Atmospheric Administration, U.S. Department of Commerce, Washington, D.C.
- Nettles, M., and Dziewonski, A.M. 2008. Radially anisotropic shear velocity structure of the upper mantle globally and beneath North America. *Journal of Geophysical Research*, **113**: B02303. doi:10.1029/2006JB004819.
- O'Hara, M.J. 1975. Is there an Icelandic mantle plume? *Nature*, **253**: 708–710.
- O'Reilly, S.Y., and Griffin, W.L. 2006. Imaging Chemical and Thermal Heterogeneity in the Sub-Continental Lithospheric Mantle: Geophysical Implications. *Tectonophysics*, **416**: 289–309.

- Oxburgh, E.R., and Parmentier, E.M. 1977. Compositional and density stratification in oceanic lithosphere: Cases and consequences. *Journal of the Geological Society*, **133**: 343–355.
- Pari, G. 2001. Crust 5.1-based inference of the Earth's dynamic surface topography: Geodynamic implications. *Geophysical Journal International*, **144**: 501–516.
- Pari, G., and Peltier, W.R. 2000. Subcontinental mantle dynamics: a further analysis based on the joint constraints of dynamic surface topography and free-air gravity. *Journal of Geophysical Research*, **105**: 5635–5662.
- Pearson, D.G. 1999. The age of the continental roots. *Lithos*, **48**: 171–194.
- Peltier, W.R., Forte, A.M., Mitrovica, J.X., and Dziewonski, A.M. 1992. Earth's gravitaitaional field: seismic tomography resolves the enigma of the Laurentian anomaly. *Geophysical Research Letters*, **19**: 1555–1558.
- Perry, H.K.C., Eaton, D.W.S., and Forte, A.M. 2002. LITH5.0: A revised crustal model for Canada based on Lithoprobe results. *Geophysical Journal International*, **150**: 285–294.
- Perry, H.K.C., Forte, A.M., and Eaton, D.W.S. 2003. Upper-mantle thermochemical structure below North America from seismic–geodynamic flow models. *Geophysical Journal International*, **154**: 279–299.
- Poudjom-Djomani, Y.H., O'Reilly, S.Y., Griffin, W.L., and Morgan, P. 2001. The density structure of subcontinental lithosphere through time. *Earth and Planetary Science Letters*, **184**: 605–621.
- Ricard, Y., and Vigny, C. 1989. Mantle dynamics with induced plate tectonics. *Journal of Geophysical Research*, **94**: 17543–17559.
- Ritsema, J., and van Heijst, H. 2000. New seismic model of the upper mantle beneath Africa. *Geology*, **28**: 63–66.
- Röhm, A.H.E., Snieder, R., Goes, S., and Trampert, J. 2000. Thermal structure of the continental upper mantle inferred from S wave velocity and surface heat flow. *Earth and Planetary Science Letters*, **181**: 395–407.
- Rudnick, R., McDonough, W.F., and O'Connell, R.J. 1998. Thermal structure, thickness and composition of continental lithosphere. *Chemical Geology*, **145**: 395–411.
- Schmidberger, S.S., and Francis, D. 1999. Nature of the mantle roots beneath the North American craton: mantle xenolith evidence from Somerset Island kimberlites. *Lithos*, **48**: 195–216.
- Schutt, D.L., and Leshner, C.E. 2006. Effects of melt depletion on the density and seismic velocity of garnet and spinel lherzolite. *Journal of Geophysical Research*, **111**: doi:10.1029/2003JB002950.
- Simmons, N.A., Forte, A.M., and Grand, S.P. 2006. Constraining mantle flow with seismic and geodynamic data: A joint approach. *Earth and Planetary Science Letters*, **246**: 109–124.
- Simmons, N.A., Forte, A.M., and Grand, S.P. 2007. Thermochemical structure and dynamics of the african superplume. *Geophysical Research Letters*, **34**: . doi:10.1029/2006GL028009.
- Simmons, N.A., Forte, A.M., and Grand, S.P. 2009. Joint seismic, geodynamic and mineral physical constraints on three-dimensional mantle heterogeneity: Implications for the relative importance of thermal versus compositional heterogeneity. *Geophysical Journal International*, **117**: 1284–1304. doi:10.1111/j.1365-246X.2009.04133.x.
- Simons, M., and Hager, B.H. 1997. Localization of gravity and the signature of glacial rebound. *Nature*, **390**: 500–504.
- Snyder, D.B., Rondenay, S., Bostock, M.G., and Lockhart, G.D. 2004. Mapping the mantle lithosphere for diamond potential using teleseismic methods. *Lithos*, **77**: 859–872.
- Sobolev, N.V. 1987. Mantle xenoliths and continental lithosphere composition. In *Composition, structure and dynamics of the lithosphere–asthenosphere system*. Edited by K. Fuchs and C. Froidevaux. AGU, Washington, D.C., Geodynamics Series, Vol. 16, pp. 161–164.
- Tackley, P.J. 2000. Mantle convection and plate tectonics: Toward an integrated physical and chemical theory. *Science*, **288**: 2002–2007.
- Tamisiea, M.E., Mitrovica, J.X., and Davis, J.L. 2007. GRACE gravity data constrain ancient ice geometries and continental dynamics over Laurentia. *Science*, **316**: 881–883.
- Turcotte, D.L., and Schubert, G. 1982. *Geodynamics: Applications of Continuum Physics to Geological Problems*. Wiley, New York, N.Y.
- Van der Lee, S., and Nolet, G. 1997. The upper mantle S-velocity structure of North America. *Journal of Geophysical Research*, **102**: 22815–22838.
- van Gerven, L., Deschamps, F., and van der Hilst, R.D. 2004. Geophysical evidence for chemical variations in the Australian continental mantle. *Geophysical Research Letters*, **31**: . doi:10.1029/2004GL020307.
- Zhao, M., Langston, C.A., Nyblade, A.A., and Owens, T.J. 1999. Upper mantle velocity structure beneath southern Africa from modeling regional seismic data. *Journal of Geophysical Research*, **104**: 4783–4794.

Appendix A. Summary of buoyancy induced mantle-flow theory

Spectral godynamic kernels

The surface topography kernel functions, $T_\ell(r)$ relate the spherical harmonic coefficients of the flow-induced surface topography $\delta\alpha_\ell^m$ to the radially varying spherical harmonic coefficients of the density contrasts $\delta\rho_\ell^m(r)$ as follows:

$$[A1] \quad \delta\alpha_\ell^m = \frac{1}{\Delta\rho_{\text{mo}}} \int_b^a T_\ell(r) \delta\rho_\ell^m(r) dr$$

In this expression, $\Delta\rho_{\text{mo}} = 2.2 \text{ Mg/m}^3$ is the density jump across the mantle–ocean boundary, a is the mean radius of the solid surface, and b is the mean radius of the core–mantle boundary (CMB). The detailed shape of the topography kernels $T_\ell(r)$ depends on the radial profile of relative (non-dimensional) mantle viscosity.

The geoid kernels $G_\ell(r)$ relate the spherical harmonic coefficients of the nonhydrostatic geoid, δN_ℓ^m , to the spherical harmonic coefficients of the density perturbations $\delta\rho_\ell^m(r)$ as follows:

$$[A2] \quad \delta N_\ell^m = \frac{3}{(2\ell + 1)\bar{\rho}} \int_b^a G_\ell(r) \delta\rho_\ell^m(r) dr$$

where $\bar{\rho} = 515 \text{ Mg/m}^3$ is the mean density of the Earth.

Free-air gravity anomalies contain two contributions: (i) the direct gravity effect due to all the density anomalies which contribute to the geoid anomalies in eq. [A2]; (ii) the indirect gravity effect which is due to the displacement between the geoid surface and the reference global surface $r = R_0 = 6371 \text{ km}$ (this displacement is, of course, the geoid undulation). This indirect effect is calculated as though there is no intervening mass between the geoid and the reference surface, hence the term “free-air” correction, which is often used to describe the indirect effect. We can show that the sum of the direct and indirect effects leads to the following expression for the free-air gravity anomalies:

$$[A3] \quad \delta G(\theta, \phi) = - \left[\frac{\partial \delta N(r, \theta, \phi)}{\partial r} \right]_{R_0} - \frac{2}{R_0} \delta N(R_0, \theta, \phi)$$

In the spherical harmonic domain, this expressions yields the following relationship between the free-air gravity anomaly coefficients δG_ℓ^m and the nonhydrostatic geoid coefficients δN_ℓ^m :

$$[A4] \quad \delta G_\ell^m = (\ell - 1) \frac{g_0}{R_0} \delta N_\ell^m$$

where $g_0 = 9.82 \text{ m/s}^2$ (982 000 mGal) is the mean gravitational acceleration at Earth's surface. In the present study, the nonhydrostatic geopotential coefficients are obtained from the EGM96 model (Lemoine et al. 1996), from which we subtract the hydrostatic rotational flattening (e.g. Jeffreys 1963; Nakiboglu 1982). Through the combination of eqs. [A2] and [A4], one can relate the gravity anomaly coefficients to the internal density perturbations.

Finally, the spherical harmonic coefficients of the flow-induced CMB topography δb_ℓ^m are related to the density perturbations $\delta \rho_\ell^m(r)$ by the CMB topography kernels $B_\ell(r)$:

$$[A5] \quad \delta b_\ell^m = \frac{1}{\Delta \rho_{\text{cm}}} \int_b^a B_\ell(r) \delta \rho_\ell^m(r) dr$$

where $\Delta \rho_{\text{cm}} = -4.43 \text{ Mg/m}^3$ is the density jump across the CMB (PREM, Dziewonski and Anderson (1981)).

The topography and geoid kernels, $T_\ell(r)$ and $G_\ell(r)$, respectively, defined in eqs. [A1] and [A2], are calculated on the basis of an effective viscosity model (Forte and Mitrovica 2001) inferred from a non-linear, iterative, Occam-style inversion of the main convection-related geophysical data. These data consist of global free-air gravity (Marsh et al. 1990) and horizontal divergence data (DeMets et al. 1990) in the degree range $\ell = 2-32$ and $\ell = 1-32$, respectively. The topography and geoid kernels, $T_\ell(r)$ and $G_\ell(r)$, calculated on the basis of the viscosity model. In the upper 200 km of the mantle, the topography kernels show peak amplitudes over all spherical harmonic degrees, however the higher degrees show more distinct, narrower peaks.

In all cases, the topography kernels achieve a value of exactly -1 at the surface, consistent with the isostatic compensation of all density anomalies located right below the solid surface through local vertical deflection of this surface. These very shallow density anomalies do not produce mantle flow. As depth increases, the density anomalies drive increasingly more flow, corresponding to reduced levels of isostatic compensation by the surface deflection and hence producing less surface topography (e.g., at $\ell > 8$, topography kernels have negligible values below about 500 km depth).

At the surface, all geoid kernels vanish because of the exact isostatic compensation of shallow mantle density anomalies. As depth increases, the kernels swing to peak negative values near 200 km depth. Density anomalies at these shallow depths interact with a very low stiffness mantle (Fig. 3) and hence produce sufficiently large mantle flow to deflect the solid surface with an amplitude large enough to overshadow the direct gravitational effect of the internal density anomalies. At greater depth, in the transition-zone region of the upper mantle, the local density anomalies interact with significantly increased stiffness of the mantle (Fig. 3). The greater viscosity of the mantle reduces the efficiency with which density anomalies drive flow, and hence the corresponding dynamic surface topography is reduced and can

no longer mask the direct gravitational effect of the internal loads at these depths. This explains the positive values of the geoid kernels (especially at short horizontal wavelengths) in the bottom half of the upper mantle and in the top of the lower mantle.

We note that constraints on density anomalies in the deepest mantle are provided by the longest wavelength (e.g., degree $\ell = 2$) components of surface topography and gravity. This implies that global-scale data are needed to properly constrain the density structure of the lower mantle.

Spatial geodynamic kernels

The spectral or wavelength-dependent geodynamic kernels $T_\ell(r)$ and $G_\ell(r)$ may also be used to represent the viscous response of the mantle in the spatial domain. We consider the derivation of the spatial kernels for the surface topography here. The surface topography, represented in spherical harmonics in eq. [A1], may be represented in geographical coordinates as follows:

$$[A6] \quad \delta a(\theta, \phi) = \sum_{\ell, m} (\delta a)_\ell^m Y_\ell^m(\theta, \phi)$$

where Y_ℓ^m is a spherical harmonic basis function of degree ℓ and order m . Similarly, the density perturbations in the mantle are expressed as a function of radius, colatitude, and longitude (r, θ, ϕ) as follows:

$$[A7] \quad \delta \rho(r, \theta, \phi) = \sum_{\ell, m} (\delta \rho)_\ell^m(r) Y_\ell^m(\theta, \phi)$$

Employing the relation

$$[A8] \quad (\delta \rho)_\ell^m(r) = \frac{1}{4\pi} \oint Y_\ell^{m*}(\theta', \phi') \delta \rho(r, \theta', \phi') dS'$$

where dS denotes integration over the entire unit sphere, and $*$ denotes complex conjugation. Combining eqs. [A1], [A7], and [A8] we obtain

$$[A9] \quad \delta a(\theta, \phi) = \frac{1}{4\pi \Delta \rho_{\text{mo}}} \int_b^a \oint \sum_{\ell, m} T_\ell(r) Y_\ell^{m*}(\theta', \phi') Y_\ell^m(\theta, \phi) \times \delta \rho(r, \theta', \phi') dS' dr$$

We use the addition theorem for spherical harmonics, which expresses a Legendre polynomial of degree ℓ in terms of a series of products of the spherical harmonics evaluated at two surface positions (θ, ϕ) and (θ', ϕ'):

$$[A10] \quad \sum_{m=-\ell}^{\ell} Y_\ell^{m*}(\theta', \phi') Y_\ell^m(\theta, \phi) = (2\ell + 1) P_\ell(\cos \Delta)$$

where the angular distance Δ between the two locations (θ, ϕ) and (θ', ϕ') is determined from the following expression:

$$[A11] \quad \cos \Delta = \cos \theta \cos \theta' + \sin \theta \sin \theta' \cos(\phi' - \phi)$$

The surface topography in eq. [A9] is represented as a function of Δ defined in eq. [A11]:

$$[A12] \quad \delta a(\theta, \phi) = \frac{1}{\Delta \rho_{\text{mo}}} \int_b^a \int_0^\pi \int_0^{2\pi} T(r, \Delta) \delta \rho(r, \theta', \phi') \times \sin \theta' d\theta' d\phi' dr$$

where $T(r, \Delta)$ is the spatial topography kernel. The general spatial representation of all geodynamic kernels is

$$[A13] \quad K(r, \Delta) = \frac{1}{4\pi} \sum_{\ell} K_{\ell}(r) P_{\ell}(\cos \Delta) (2\ell + 1)$$

where $K(r, \Delta)$ are the spatial kernels and $K_{\ell}(r)$ is the associated spectral kernel corresponding to either dynamic topography or free-air gravity.

The geoid anomalies in geographic coordinates are expressed as

$$[A14] \quad \delta N(\theta, \phi) = \frac{3}{\bar{\rho}} \int_b^a \int_0^{\pi} \int_0^{2\pi} N(r, \Delta) \delta \rho(r, \theta', \phi') \times \sin \theta' d\theta' d\phi' dr$$

where $N(r, \Delta)$ is the spatial geoid kernel. The corresponding free-air gravity anomalies are

$$[A15] \quad \delta G(\theta, \phi) = \frac{3g_0}{\bar{\rho}R_0} \int_b^a \int_0^{\pi} \int_0^{2\pi} G(r, \Delta) \delta \rho(r, \theta', \phi') \times \sin \theta' d\theta' d\phi' dr$$

The spatial kernels (Fig. A1) employed are calculated by summing the spectral kernels for a no-slip surface boundary condition. This surface boundary condition is appropriate for describing the interaction of upper mantle density anomalies with an overlying plate. The depth-dependent behaviour of the spatial kernels reflects the radial variation in the spectral kernels.

Both the topography and free-air gravity kernel amplitudes are dominant in the upper mantle, decreasing to very small relative amplitude below about 500 km. The kernels are represented as a function of Δ , at different depths, in Fig. A2. The topography kernels have a peak (negative) amplitude at the top of the mantle (Fig. A2a), decreasing in magnitude to ~ 670 km depth. The free-air gravity kernels (Figs. A2d–A2f) show zero amplitude at the surface, a peak (negative) amplitude at ~ 93 km depth (Fig. A2e), and then change sign to positive values at ~ 272 km depth (Fig. A2f).

As discussed earlier, the change in sign of the gravity kernels reflects the interaction of local density anomalies with increasingly stiffer, sluggish mantle below ~ 250 km depth. At still greater depth, the local density anomalies corresponding to short wavelengths provide less surface gravity signal, as reflected by the decrease to very small values of the spatial gravity kernels below ~ 800 km depth.

In summary, the regional dynamic surface topography is very useful in determining the buoyancy properties of the shallow lithospheric mantle, since its spatial response functions peak at the Earth's solid surface. In contrast, the free-air gravity-response functions vanish at the solid surface and achieve peak amplitudes toward 100 km depth. This implies that the regional gravity anomalies will provide strongest constraints on the buoyancy of the deeper continental lithosphere.

Truncation of the geodynamic kernels

In expressions [A12]–[A15], the angular distance Δ between two geographic coordinates (θ, ϕ) and (θ', ϕ') , extends from 0° to 180° at the antipode of (θ, ϕ) . Spatial convolution of the density structure with the kernels over all θ and ϕ is, therefore, computationally intensive. We truncate the spatial topography and free-air gravity kernels (Fig. A2a–A2f) at Δ

$= 30^\circ$, since the accuracy is not significantly improved using a wider window. Since most of the amplitude of the kernels is focused around $\Delta = 0^\circ$, beyond which the amplitudes decrease rapidly to small relative values, truncation is valid. Small but persistent errors are incurred, however, because of the relatively small-amplitude oscillatory undulations of the kernels out to $\Delta = 180^\circ$. Error associated with the truncation is assessed through comparison of the spatial representation of geodynamic fields up to harmonic degree and order $\ell = 128$, and those calculated in the truncated spatial domain using the spatial kernels. The spherical harmonic expansions up to this degree and order are accurate representations of all the information contained in the geodynamic kernels, and thus their comparison to the results obtained using the truncated kernels reveals the extent of the error incurred by truncating at 30° . The resulting root mean square (rms) difference between the dynamic topography and free-air gravity anomalies computed in the spatial domain using the tomography model of Grand (2002) and those calculated on the basis of a spherical harmonic expansion up to degree and order $\ell = 128$ for the same tomography model are 5% and 7%, respectively.

Our use of degree-128 spatial kernels is based on the requirement that the regional (North American) data should be employed to constrain the regional mantle heterogeneity directly below the continent. As discussed earlier, the horizontal integration width of the degree-128 kernels meets this requirement.

Kogan and McNutt (1993) present an alternative method for truncating the geodynamic kernels, and we performed a second test of the validity of our kernel truncations by comparing our results to those obtained using their methodology. To calculate the spatial topography kernels, Kogan and McNutt (1993) truncate the kernels expressed in the spectral domain, thereby defining a null space for the spatial convolution. Since we are working on a regional scale (characterized by half wavelengths ≤ 1500 km), we may confine the analysis to harmonic degrees $\ell = 12$ since the longer wavelengths would require a whole Earth treatment. Following Kogan and McNutt, an arbitrary combination of the first 11 Legendre polynomials may be subtracted from the spherical harmonic expansions (eq. [A13]) of the kernels. The results obtained using this methodology are in agreement with those found using our truncation method in the spatial domain.

References

- DeMets, C.R., Gordon, R.G., Argus, D.F., and Stein, S. 1990. Current plate motions. *Geophysical Journal International*, **101**: 425–478.
- Dziewonski, A.M., and Anderson, D.L. 1981. Preliminary reference Earth model. *Physics of the Earth and Planetary Interiors*, **25**: 297–356.
- Forte, A.M., and Mitrovica, J.X. 2001. Deep-mantle high-viscosity flow and thermochemical structure inferred from seismic and geodynamic data. *Nature*, **410**: 1049–1056.
- Grand, S.P. 2002. Mantle shear-wave tomography and the fate of subducted slabs. *Philosophical Transactions of the Royal Society of London. Series A: Mathematical and Physical Sciences*, **360**: 2475–2491.
- Jeffreys, H. 1963. On the hydrostatic theory of the figure of the Earth. *Geophysical Journal of the Royal Astronomical Society*, **8**: 196–202.
- Kogan, M.G., and McNutt, M.K. 1993. Gravity field over northern

Fig. A1. (a) Spatial topography kernels and (b) free-air gravity kernels represented as a function of depth in the mantle, for the viscosity profile defined in Fig. 3 (Forte and Mitrovica 2001). The kernels are calculated using eq. [A13], where $\Delta = 0$ and $\ell_{\max} = 128$.

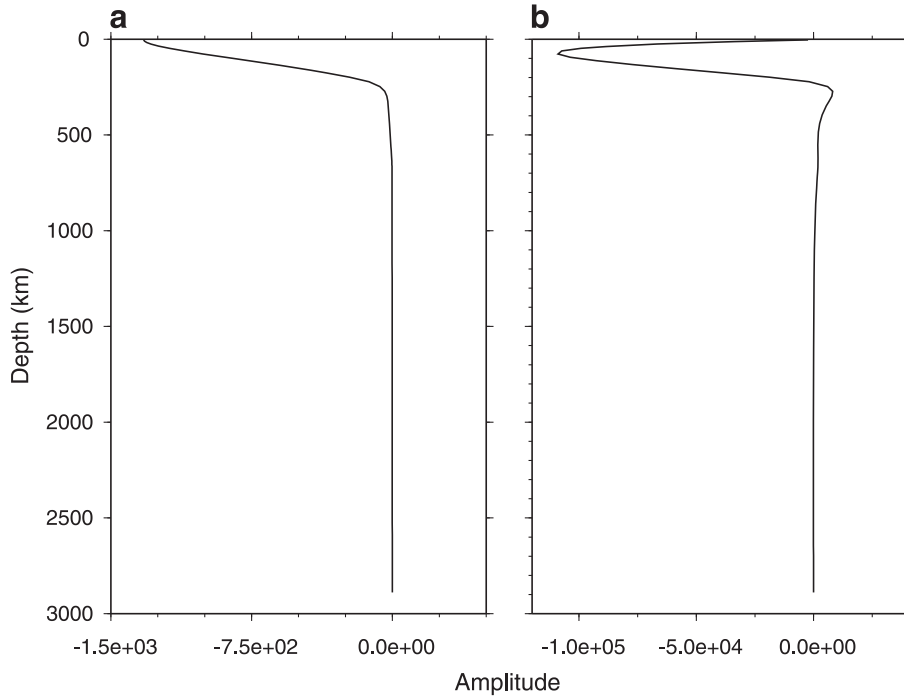
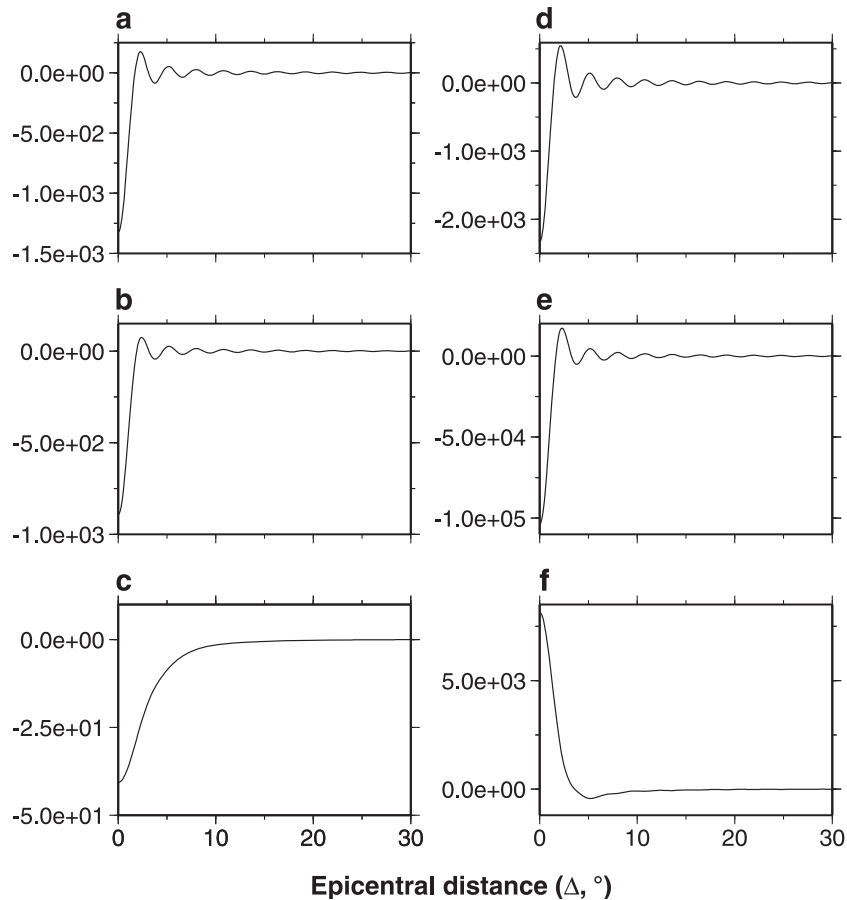


Fig. A2. Spatial topography and free-air gravity kernels represented as a function of epicentral distance, Δ , calculated on the basis of the viscosity profile defined in Fig. 3. (a–c) Topography kernels at depths 3, 93, and 272 km in the mantle, respectively. (d–f) Free-air gravity kernels at depths 3, 93, and 272 km in the mantle, respectively.



Eurasia and variations in the strength of the upper mantle. *Science*, **259**: 473–479.

Lemoine, F.G., Kenyon, S.C., Factor, J.K., Trimmer, R.G., Pavlis, N.K., Chinn, D.S., et al. 1996. The development of the joint NASA GSFC and NIMA geopotential model EGM96. NASA Goddard Space Flight Center, Greenbelt, Md., USA.

Marsh, J.G., Lerch, F.J., Putney, B.H., Felsentreger, T.L., Sanchez, B.V., Klosko, S.M., et al. 1990. The GEM-T2 gravitational model. *Journal of Geophysical Research*, **95**: 22 043–22 071.

Nakiboglu, S.M. 1982. Hydrostatic theory of the Earth and its mechanical implications. *Physics of the Earth and Planetary Interiors*, **28**: 302–311.

Appendix B. Thermochemical structure of the tectosphere

The effects of lateral variations in temperature and composition on variations in seismic shear-wave velocity ($\delta V_s/V_s$) and density ($\delta\rho/\rho$) in the tectosphere may be expressed by

$$[B1] \quad \frac{\delta\rho}{\rho} = -\alpha\delta T + \frac{\partial\ln\rho}{\partial R}\delta R + \frac{\partial\ln\rho}{\partial X_{Gt}}\delta X_{Gt}$$

$$[B2] \quad \frac{\delta V_s}{V_s} = \frac{\partial\ln V_s}{\partial T}\delta T + \frac{\partial\ln V_s}{\partial R}\delta R + \frac{\partial\ln V_s}{\partial X_{Gt}}\delta X_{Gt}$$

where δT are the temperature perturbations, and, following the method of Jordan (1979), the compositional heterogeneity is expressed in terms of the iron molar ratio, $R = X_{Fe}/(X_{Fe} + X_{Mg})$ and the molar fraction of garnet in the whole rock, X_{Gt} . Using the estimates of Jordan (1979)

$$[B3] \quad \frac{\partial\ln V_s}{\partial R} = -0.34, \quad \frac{\partial\ln V_s}{\partial X_{Gt}} = +0.05$$

$$[B4] \quad \frac{\partial\ln\rho}{\partial R} = +0.32, \quad \frac{\partial\ln\rho}{\partial X_{Gt}} = +0.10$$

and assuming 10% fractionation of basalt from fertile subcontinental lherzolite, for which $\delta R \approx -0.013$ and $\delta X_{Gt} \approx -0.056$ (see table 6 in Jordan (1979)), yields the following compositional perturbations:

$$[B5] \quad \frac{\delta V_s}{V_s} = +0.16\%, \quad \frac{\delta\rho}{\rho} = -0.98\%$$

Assuming a temperature perturbation of -500 °C at 100 km depth (Jaupart and Mareschal 1999) yields the following thermal perturbations:

$$[B6] \quad \frac{\delta V_s}{V_s} = -7.0\%, \quad \frac{\delta\rho}{\rho} = +1.75\%$$

where we take $\alpha = 3.5 \times 10^{-5} \text{ K}^{-1}$ and $\partial\ln V_s/\partial T = -14 \times 10^{-5} \text{ K}^{-1}$ (Karato 1993).

On the basis of expressions eqs. [B1] and [B2], we obtain

$$[B7] \quad \left(\frac{\delta\rho}{\rho}\right)_{sh} = -\alpha\delta T + A\delta R = \left(\frac{d\ln\rho}{d\ln V_s}\right)_{sh} \left(\frac{\delta V_s}{V_s}\right)_{sh}$$

$$[B8] \quad \left(\frac{\delta V_s}{V_s}\right)_{sh} = -\alpha \left(\frac{d\ln V_s}{d\ln\rho}\right)_{th} \delta T + B\delta R$$

where

$$A = \frac{\partial\ln\rho}{\partial R} + \frac{\partial\ln\rho}{\partial X_{Gt}} \frac{\delta X_{Gt}}{\delta R}$$

$$[B9] \quad B = \frac{\partial\ln V_s}{\partial R} + \frac{\partial\ln V_s}{\partial X_{Gt}} \frac{\delta X_{Gt}}{\delta R}$$

We estimate a value for $\frac{\delta X_{Gt}}{\delta R}$ by considering the covariance between whole-rock depletion of iron and garnet, which may be estimated from models of basalt extraction from a pyrolite starting composition. The estimates provided by Jordan (1979) (see fig. 1 and table 6) for the effect of 10% partial melting yield $\frac{\delta X_{Gt}}{\delta R} \approx 4$. The coefficient of thermal expansion, α , is assumed to vary linearly from $3.3 \times 10^{-5} \text{ K}^{-1}$ at the top of the mantle to $2.5 \times 10^{-5} \text{ K}^{-1}$ at the bottom of the upper mantle.

Solving for δT and δR yields

$$[B10] \quad \delta T = -\frac{1}{\alpha} \left(\frac{d\ln\rho}{d\ln V_s}\right)_{sh} \left[\left(\frac{d\ln V_s}{d\ln\rho}\right)_{sh} - \frac{B}{A} \right] \times \left[\left(\frac{\partial\ln V_s}{\partial\ln\rho}\right)_{th} - \frac{B}{A} \right]^{-1} \left(\frac{\delta V_s}{V_s}\right)_{sh}$$

$$[B11] \quad \delta R = \frac{1}{A} \left[\left(\frac{\partial\ln V_s}{\partial\ln\rho}\right)_{th} \left(\frac{d\ln\rho}{d\ln V_s}\right)_{sh} - 1 \right] \times \left[\left(\frac{\partial\ln V_s}{\partial\ln\rho}\right)_{th} - \frac{B}{A} \right]^{-1} \left(\frac{\delta V_s}{V_s}\right)_{sh}$$

Exterior to the tectosphere (i.e., in the ‘thermal’ mantle), compositional heterogeneity is assumed to be negligible and thermal heterogeneity is the primary cause of the seismic velocity anomalies. In these regions we have

$$[B12] \quad \left(\frac{\delta\rho}{\rho}\right)_{th} = \alpha\delta T = \left(\frac{d\ln\rho}{d\ln V_s}\right)_{th} \left(\frac{\delta V_s}{V_s}\right)_{th}$$

$$\delta T = -\frac{1}{\alpha} \left(\frac{d\ln\rho}{d\ln V_s}\right)_{th} \left(\frac{\delta V_s}{V_s}\right)_{th}$$

References

- Jaupart, C., and Mareschal, J.-C. 1999. The thermal structure and thickness of continental roots. *Lithos*, **48**: 93–114.
- Jordan, T.H. 1979. The mantle sample: Inclusions in kimberlites and other volcanics. *In Proceedings of the 2nd International Kimberlite Conference. Edited by F.R. Boyd and H. Meyer.* AGU, Washington, D.C., pp. 1–14.
- Karato, S.I. 1993. The importance of anelasticity in the interpretation of seismic tomography. *Geophysical Research Letters*, **20**: 1623–1626.